ADVANCED
FUNCTIONAL
MATERIALS

# Supporting Information

for *Adv. Funct. Mater.,* DOI: 10.1002/adfm.202102530

# Layer-by-Layer Assembly-Based Electrocatalytic Fibril Electrodes Enabling Extremely Low Overpotentials and Stable Operation at 1 A cm$^{-2}$ in Water-Splitting Reaction

*Younji Ko, Jinho Park, Jeongmin Mo, Seokmin Lee, Yongkwon Song, Yongmin Ko, Hoyoung Lee, Yongju Kim, June Huh, Seung Woo Lee,* and Jinhan Cho**

Supporting Information

# Layer-by-Layer Assembly-Based Elecrocatalytic Fibril Electrodes Enabling Extremely Low Overpotentials and Stable Operation at 1 A·cm$^{-2}$ in Water-Splitting Reaction

*Younji Ko, Jinho Park, Jeongmin Mo, Seokmin Lee, Yongkwon Song, Yongmin Ko, Hoyoung Lee, Yongju Kim, June Huh, Seung Woo Lee*, and Jinhan Cho**

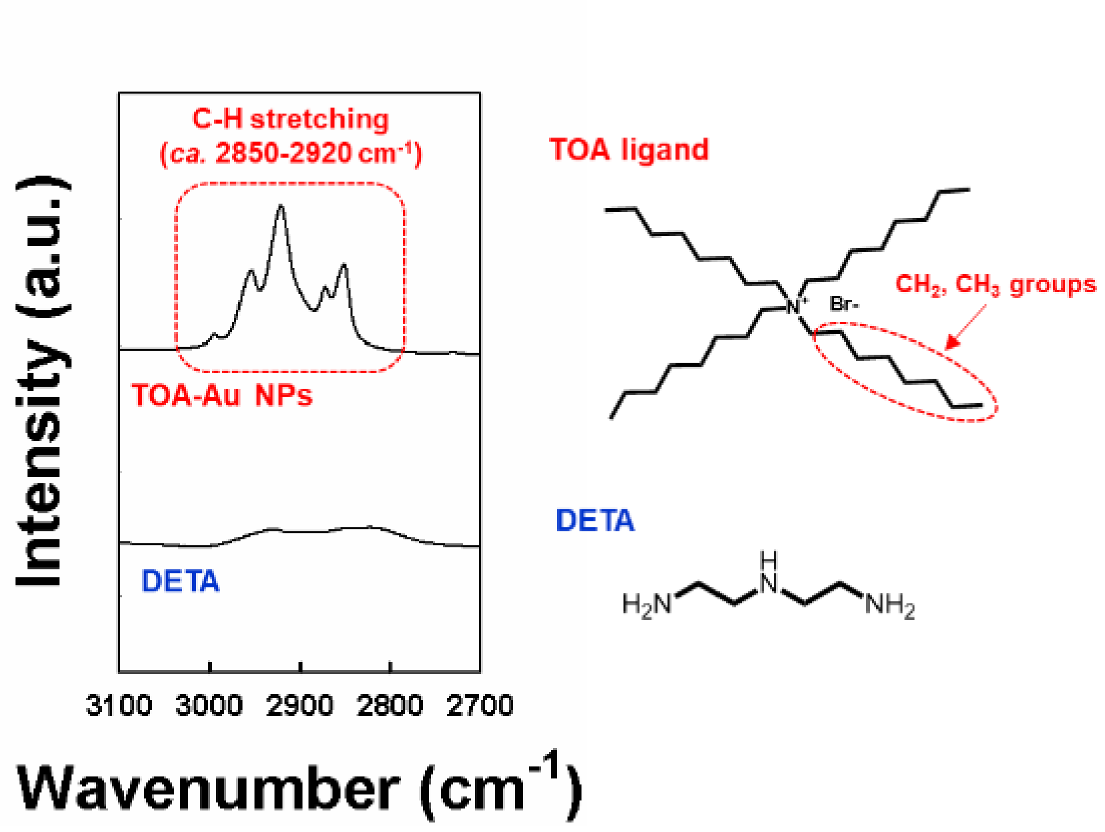

**Figure S1.** FTIR spectra of the TOA-Au NPs and DETA. The TOA-Au NPs showed C–H stretching peaks derived from the long alkyl chains of the ligands in the range from 3000 to 2850 $cm^{-1}$, whereas DETA did not show any absorbance peak in this range.

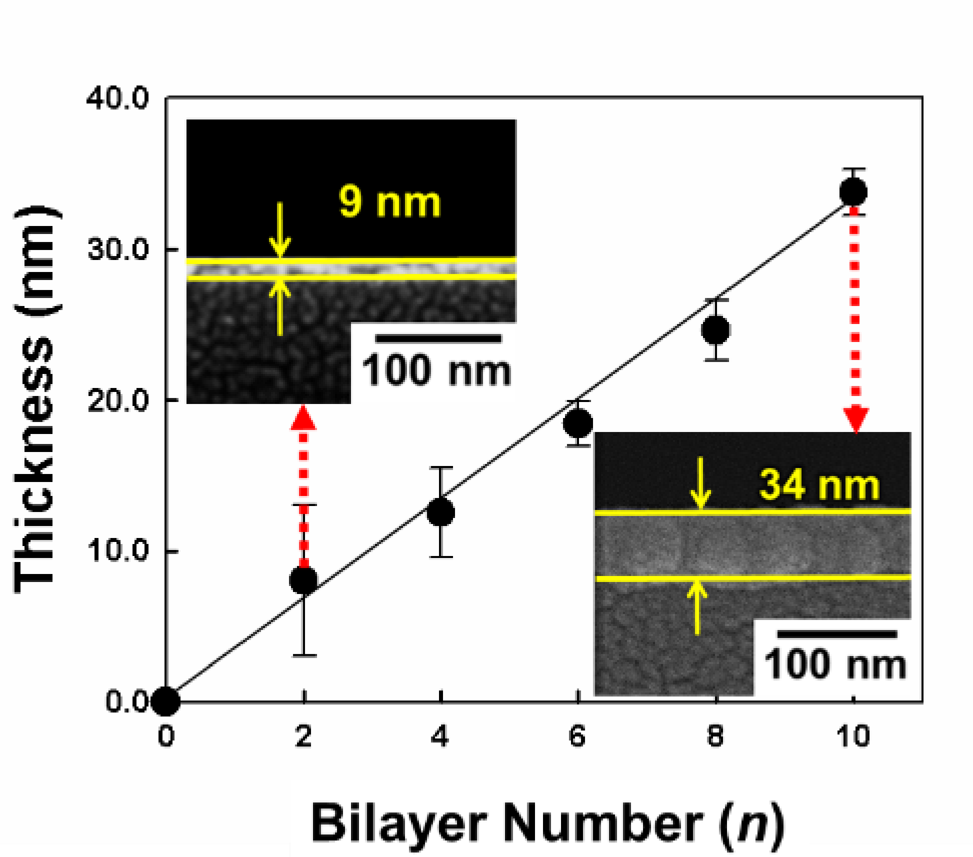

**Figure S2.** Film thickness of (TOA-Au NP/DETA)$_n$ multilayers. The film thickness increased with increasing bilayer number from 1 to 10. The inset shows cross-sectional FE-SEM images and the total thickness of the (TOA-Au NP/DET(A)$_n$ multilayers.

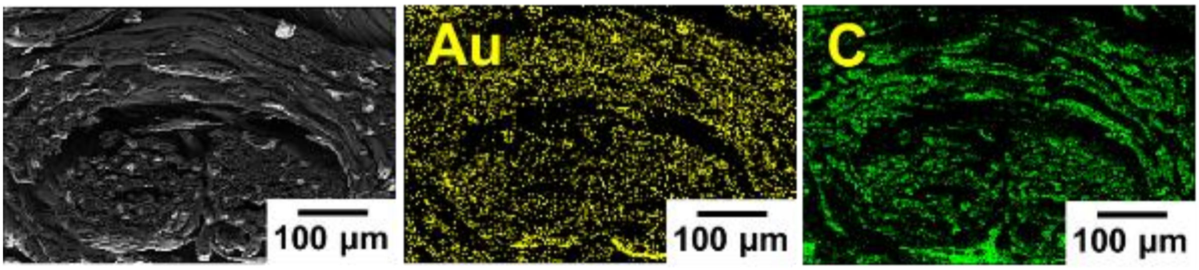

**Figure S3.** Cross-sectional FE-SEM and EDX mapping images of the (TOA-Au/DETA)$_4$-coated cotton electrode.

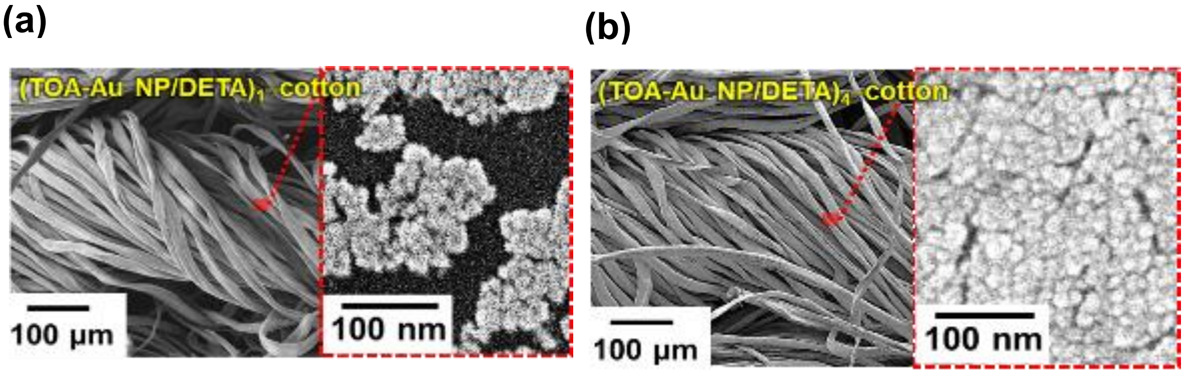

**Figure S4.** FE-SEM images of a) (TOA-Au NP/DETA)$_{n=1}$− and b) (TOA-Au NP/DETA)$_{n=4}$ −coated cotton textiles.

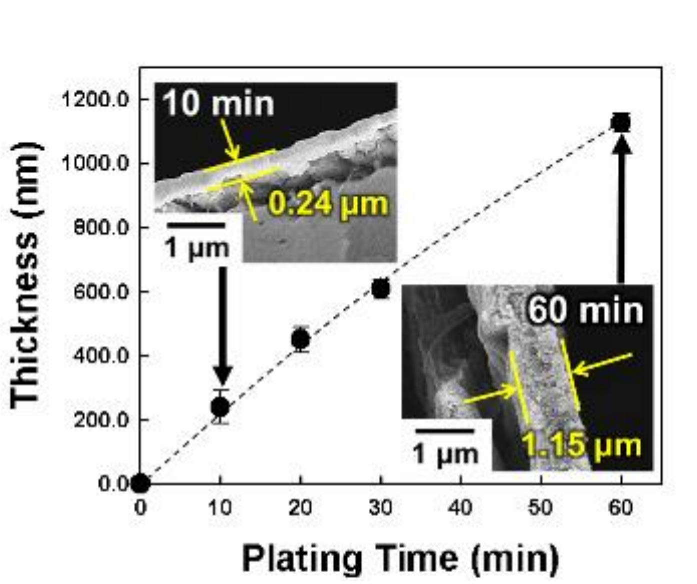

**Figure S5.** Thickness and FE-SEM images (insets) of the electroplated Ni layer onto EP Ni-fiber (within the EP Ni–cotton) as a function of electroplating time at a current density of 346 mA $cm^{-2}$.

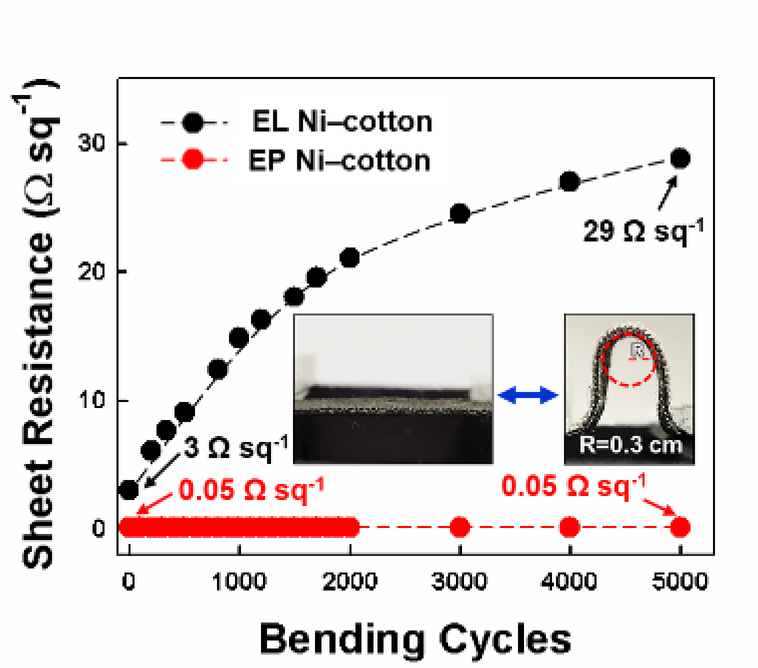

**Figure S6.** Mechanical stability tests for the EP Ni–cotton and EL Ni–cotton as a function of the bending cycling number (bending radius of ~ 0.3 cm). In the case of EP Ni–cotton, its sheet resistance was maintained without any significant change despite the repeated bending cycle tests (at least 5000 times), and on the other hand the sheet resistance of EL Ni–cotton continuously increased.

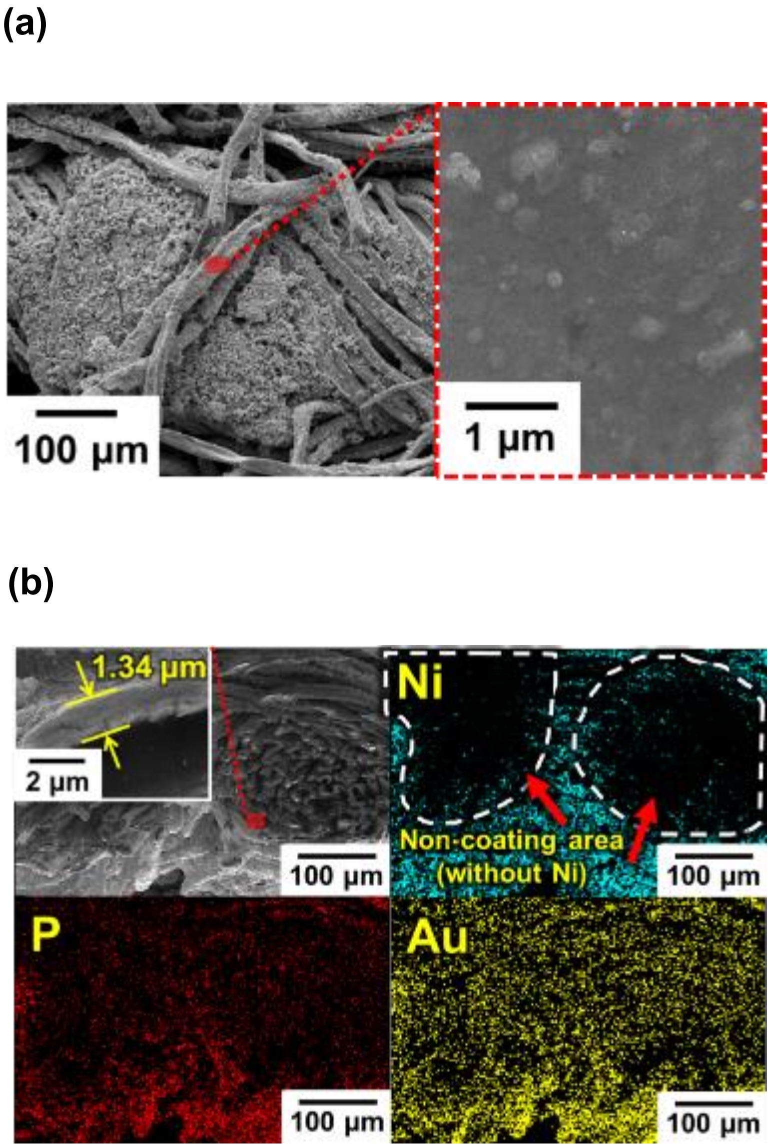

**Figure S7.** a) Planar FE-SEM images and b) cross-sectional EDX mapping image of the EL Ni–cotton electrode prepared from the (TOA-Au NP/DETA)$_4$ multilayers-coated cotton.

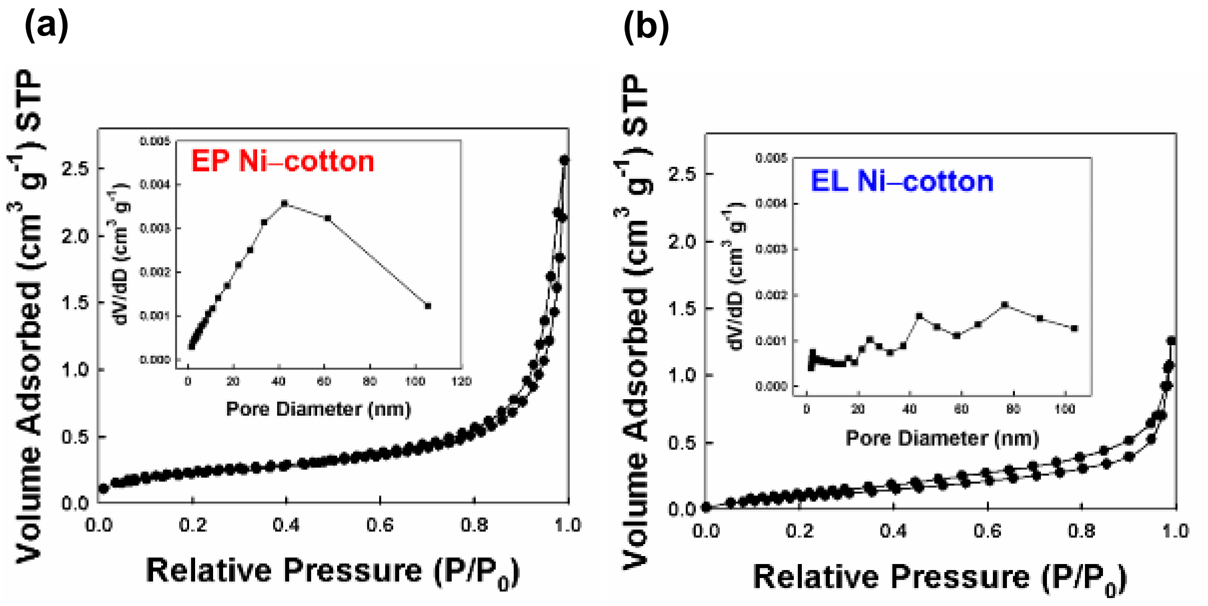

**Figure S8.** $N_2$ adsorption-desorption isotherms, and pore size distributions of a) EP Ni–cotton, and b) EL Ni–cotton. In this case, the pore size in the EP Ni–cotton was distributed in the range from ~1 to ~110 nm with a distinct peak at 42.5 nm, which is more uniform pore formation than that of EL Ni–cotton (i.e., 2.6, 24.4,43.6, and 76.5 nm). Moreover, the specific surface area of the EP Ni–cotton was measured to be 0.869 m$^2$ g$^{-1}$, which was approximately 2 times higher than that of the EL Ni–cotton (0.469 m$^2$ g$^{-1}$). This increased specific surface of the EP Ni–cotton was mainly attributed to the large amount of Ni protrusions created during the electroplating.

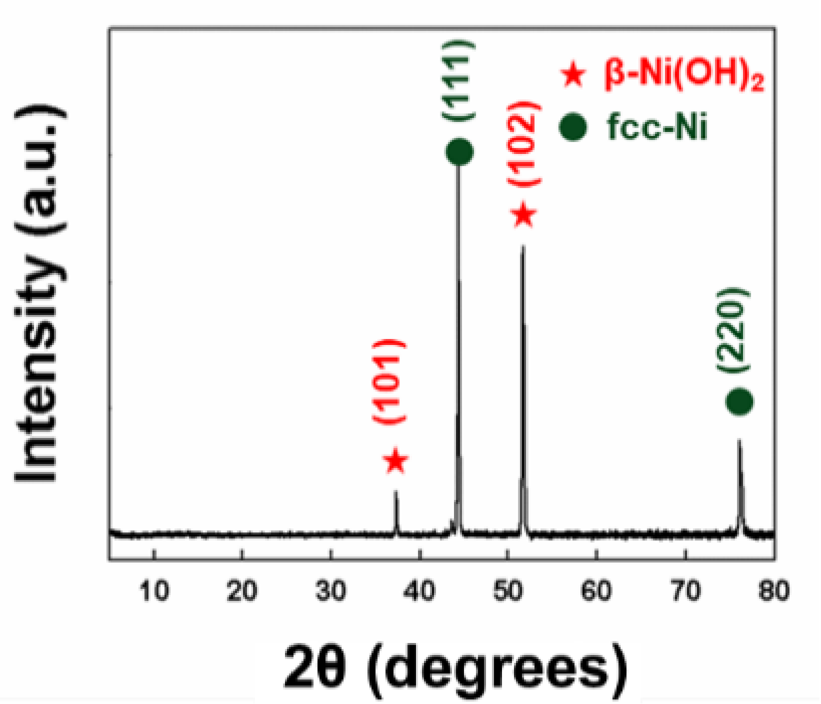

**Figure S9.** The XRD pattern of the Ni foam exhibited the characteristic (101) and (102) peaks of β-$Ni(OH)_2$ and (111) and (220) peaks of fcc-Ni.[S1]

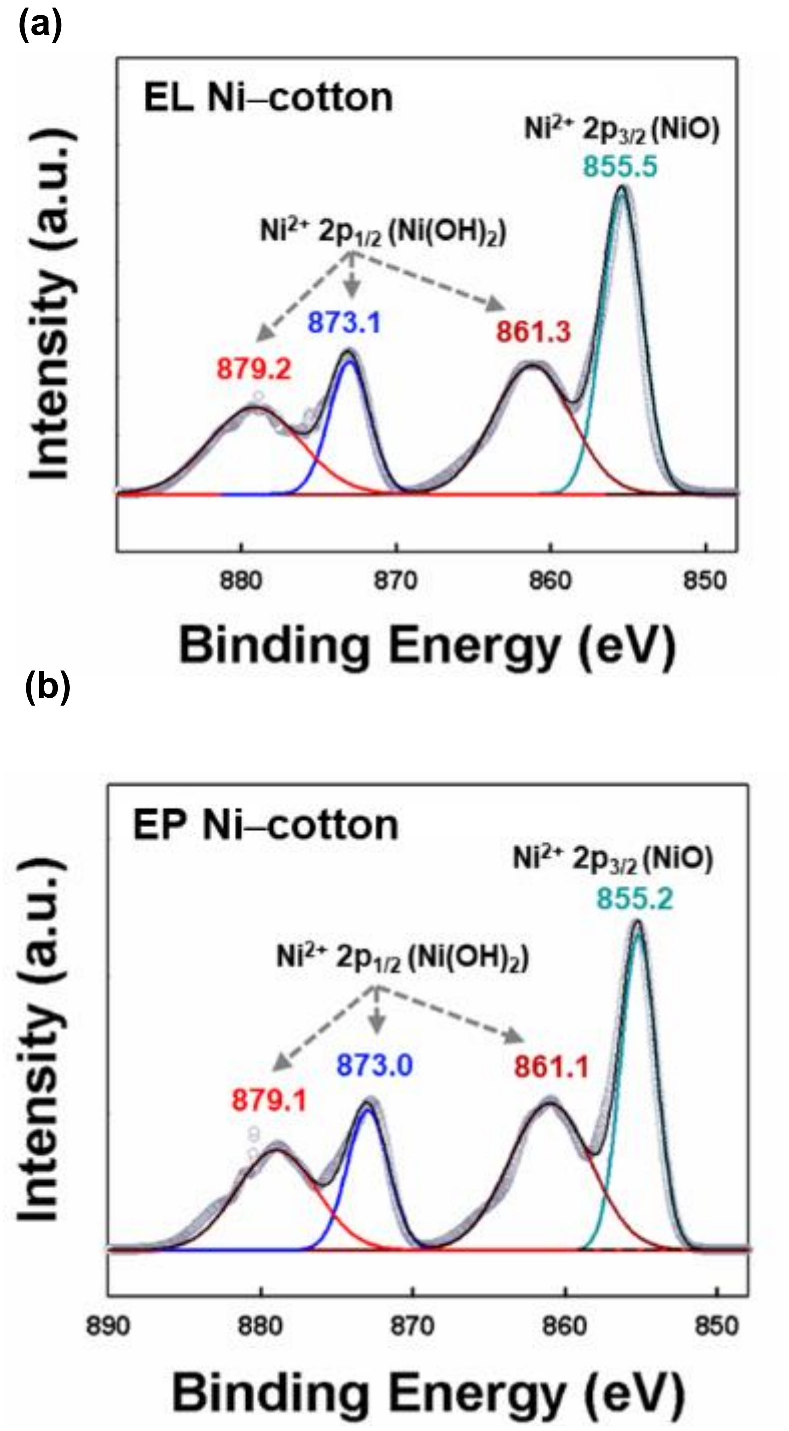

**Figure S10.** XPS spectra of a) the EL Ni–cotton (electroless deposition) electrode and b) the EP Ni–cotton (electroplating deposition).

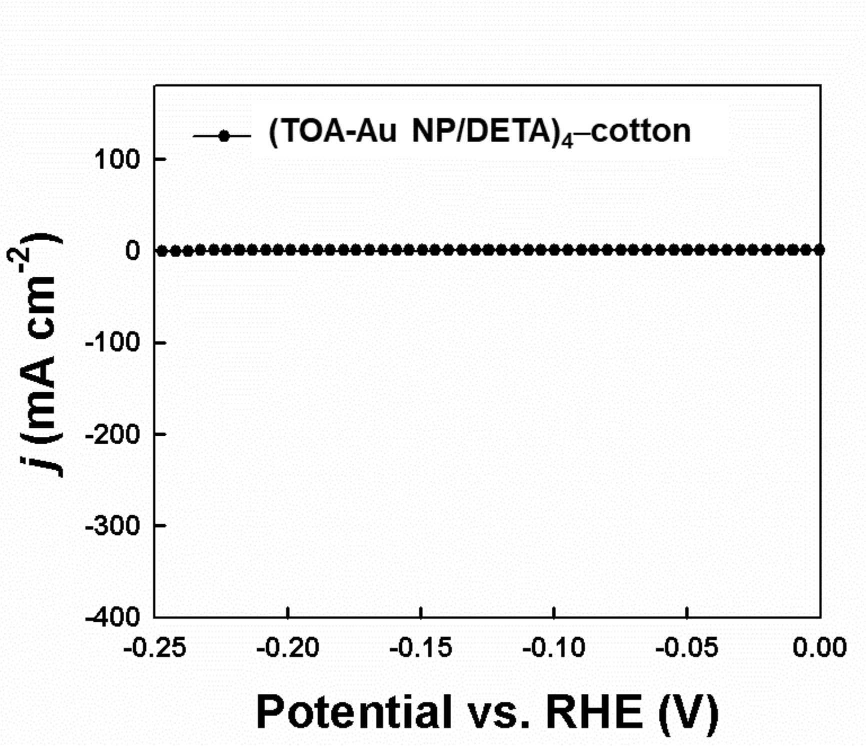

**Figure S11.** HER polarization curve of the (TOA-Au NP/DETA)$_4$-coated cotton (before Ni electroplating) measured in Ar-saturated 1 M KOH.

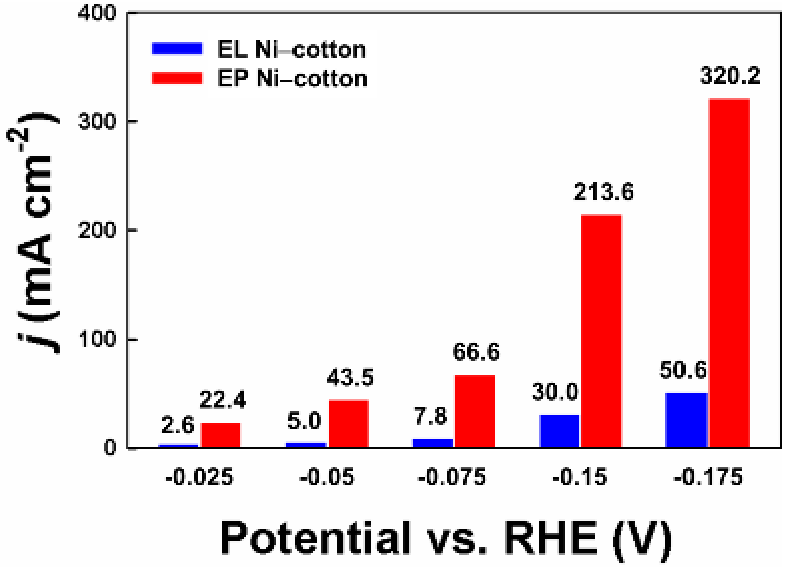

**Figure S12.** Change in current densities (*j*) of the EP Ni– and the EL Ni–cotton with increasing the potential.

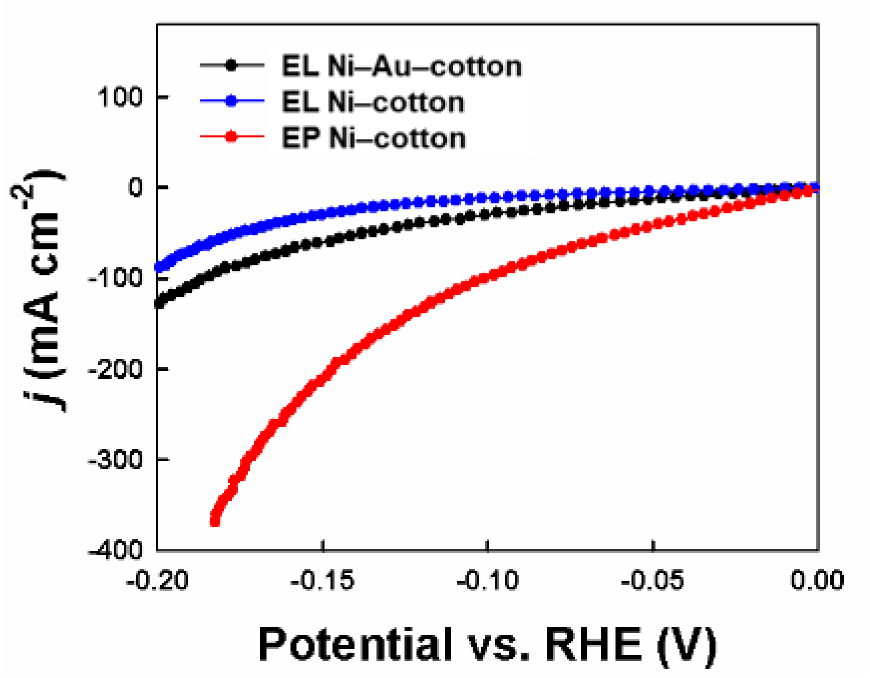

**Figure S13.** HER polarization curves of EL Ni–Au–cotton, EL Ni–cotton, and EP Ni–cotton measured in Ar-saturated 1 M KOH. In this case, EL Ni–Au–cotton implies the EL Ni–cotton electrode with the (TOA-Au NP/DETA)$_4$ multilayers. The sheet resistance (approximately 3 $\Omega$ sq$^{-1}$) of EL Ni–Au–cotton was almost identical to that of EL Ni–cotton.

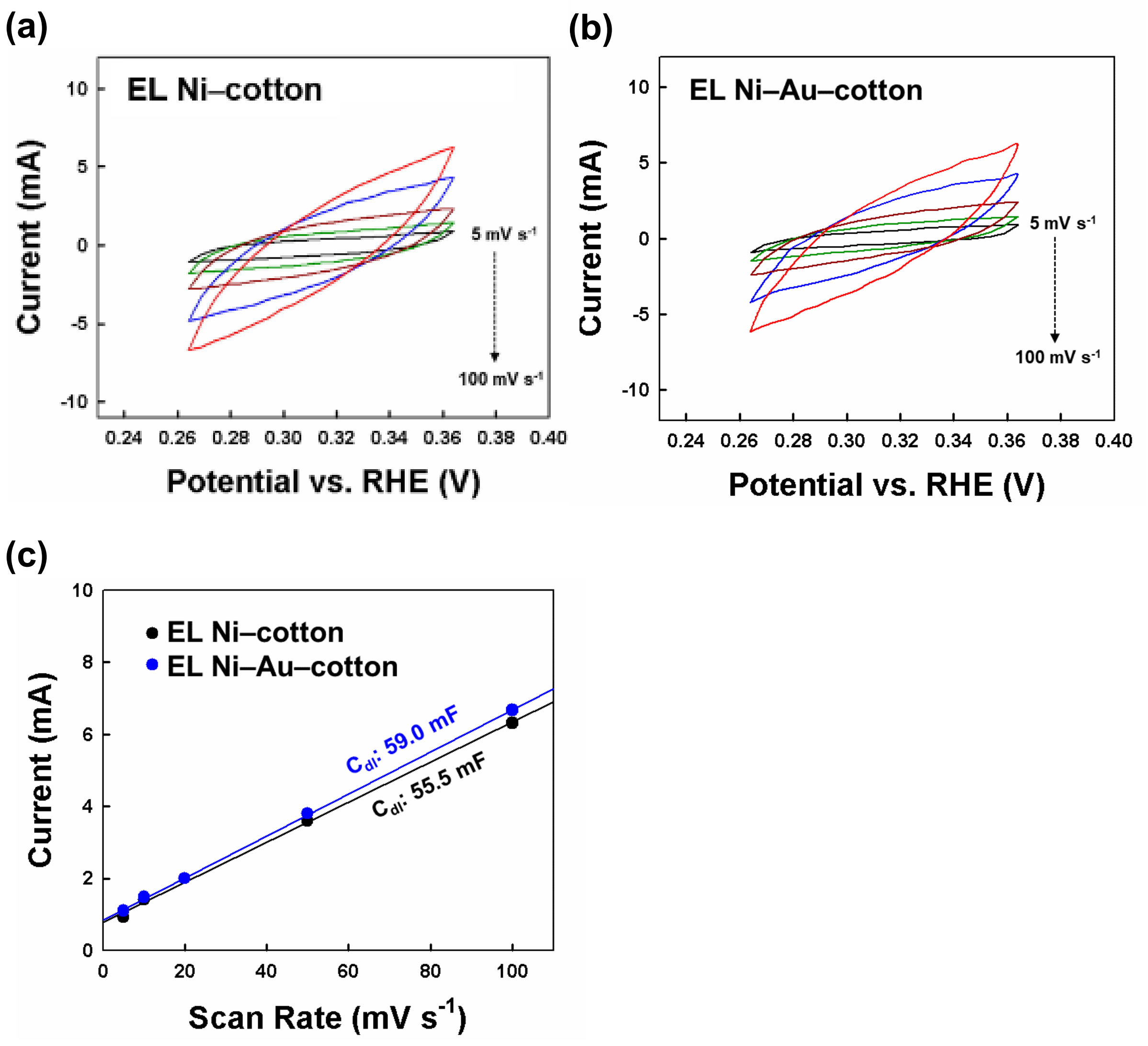

**Figure S14.** CV curves recorded in the non-faradaic region (0.26–0.36 V) at different scan rates (5, 10, 20, 50, and 100 mV $s^{-1}$) for a) EL Ni–cotton (electroless deposition) (i.e., 138 mM Ni precursor concentration) and b) EL Ni–Au–cotton. c) Double-layer capacitance ($C_{dl}$) for the electrodes measured at different scan rates. In this case, EL Ni–Au–cotton is defined as a EL Ni–cotton electrode including the (TOA-Au NP/DETA)$_4$ multilayers. Based on the specific capacitance of 0.040 mF $cm^{-2}$ of Ni, the ECSA of the EL Ni–cotton and EL Ni–Au–cotton electrode were calculated to be approximately 1387.5 $cm^2$ and 1475 $cm^2$, respectively.

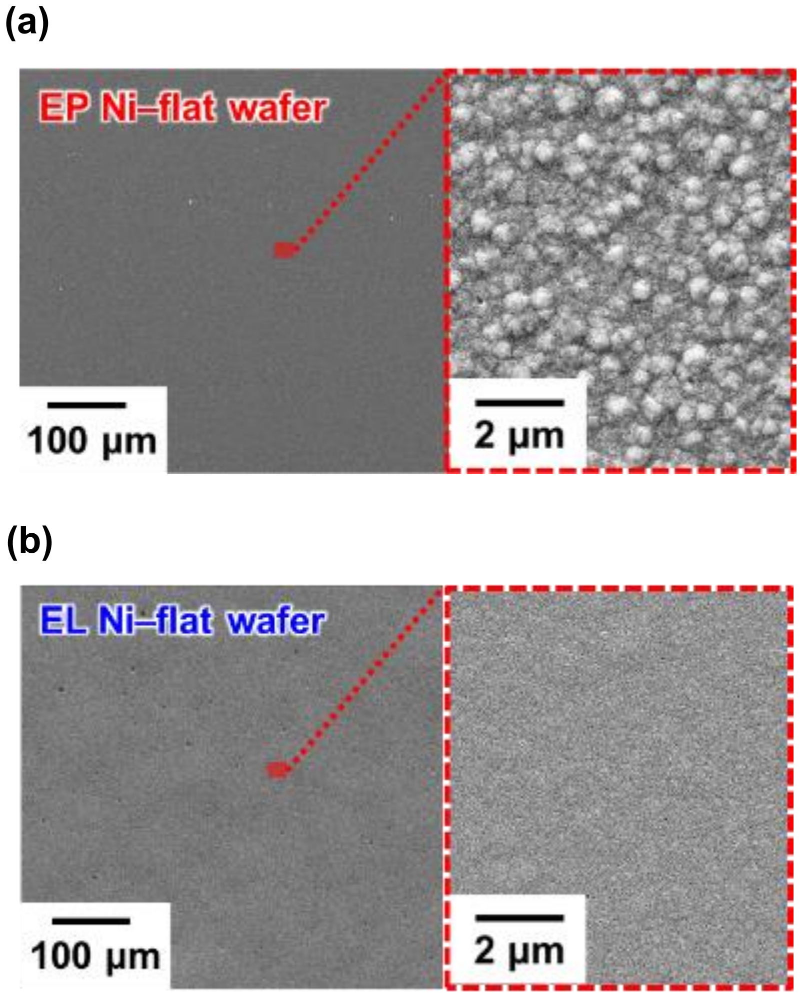

**Figure S15.** FE-SEM images of a) EP Ni–flat Si wafer and b) EL Ni–flat Si wafer.

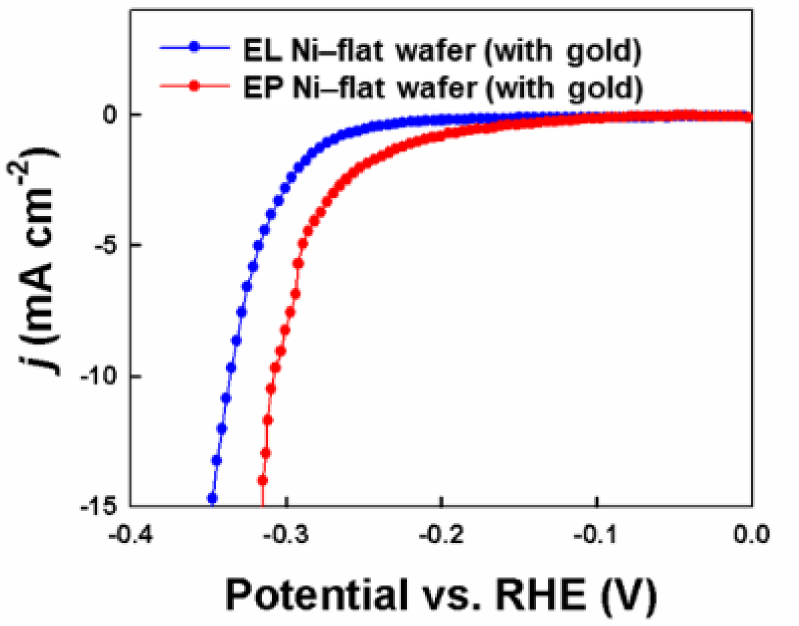

**Figure S16.** HER polarization curves of EP Ni– and EL Ni–flat Si wafer (with gold) measured in Ar-saturated 1 M KOH.

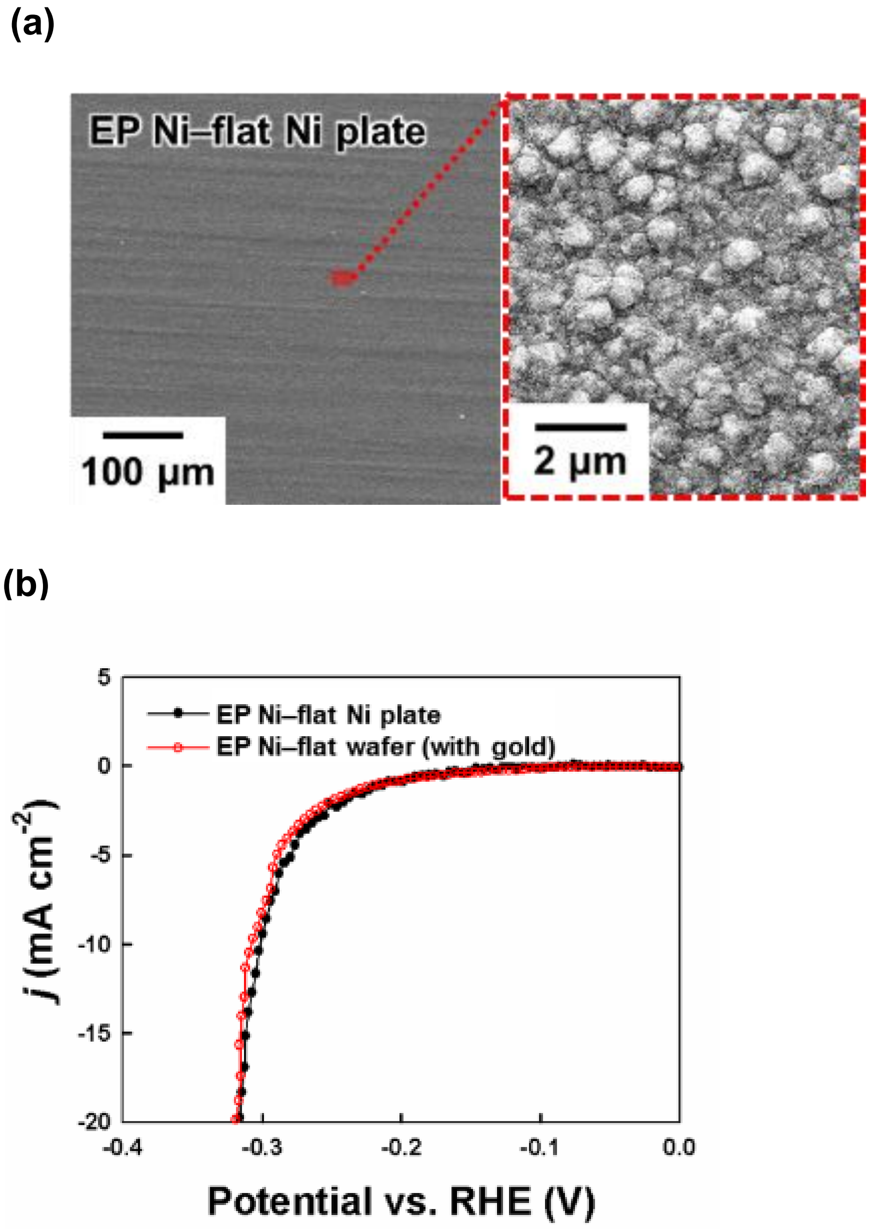

**Figure S17.** a) FE-SEM image and b) HER polarization curve of EP Ni–flat Ni plate and EP Ni–flat Si wafer (with gold). In this case, the HER performance was measured in Ar-saturated 1 M KOH.

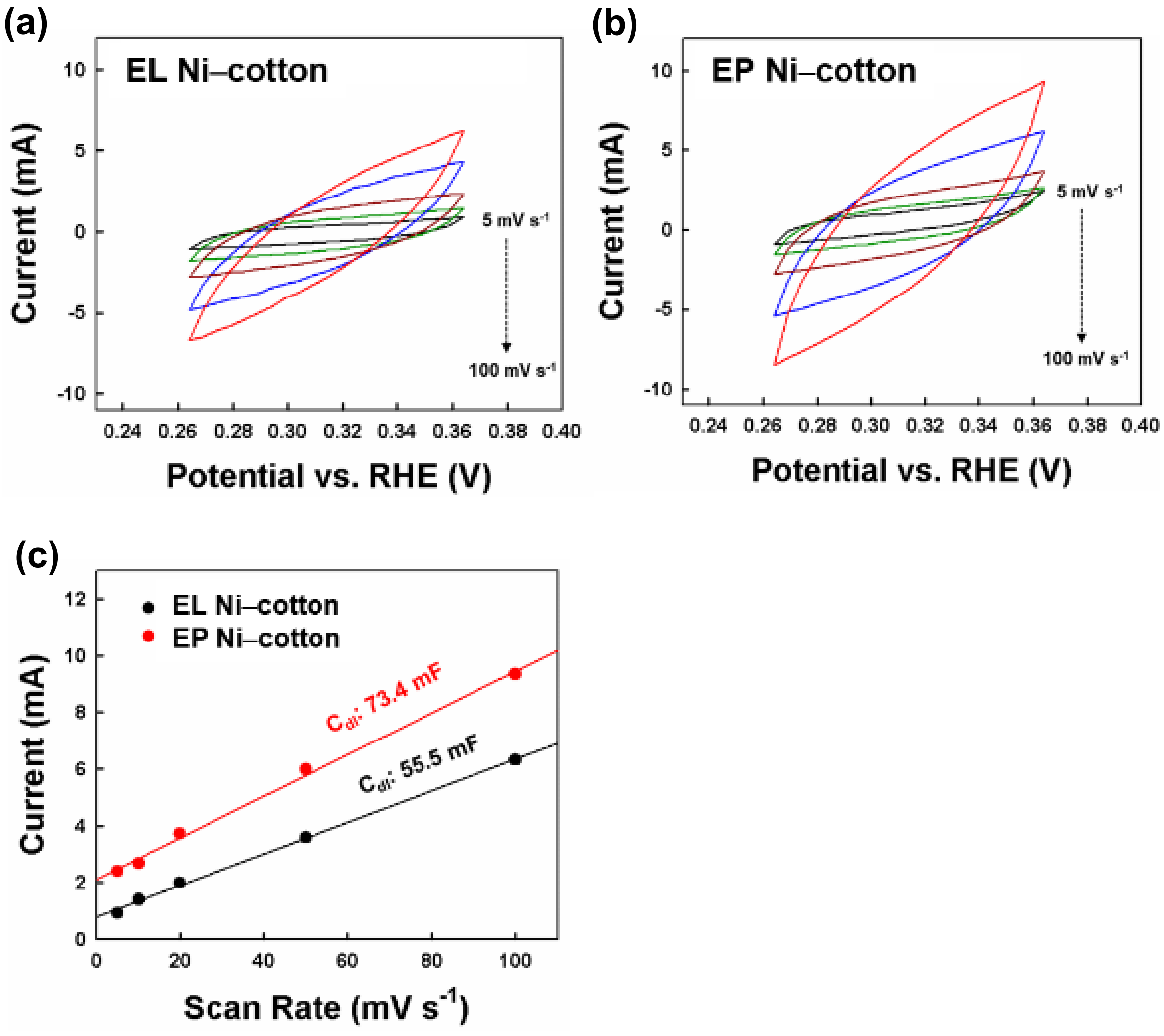

**Figure S18.** CV curves recorded in the non-faradaic region (0.26–0.36 V) at different scan rates (5, 10, 20, 50 and 100 mV $s^{-1}$) for a) EL Ni–cotton (electroless deposition) (i.e., 138 mM Ni precursor concentration) and b) EP Ni–cotton (electroplating deposition). c) Double-layer capacitance ($C_{dl}$) for the electrodes measured at different scan rates.

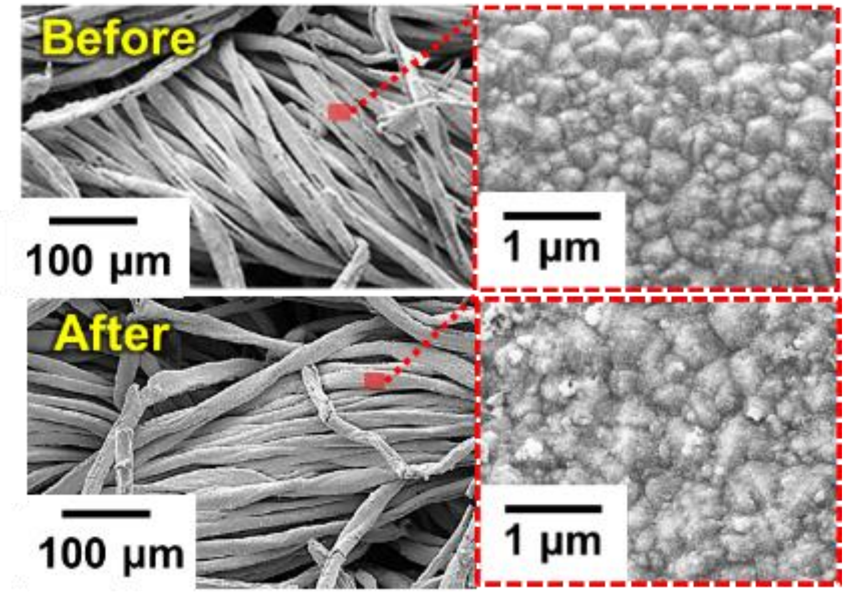

**Figure S19.** Planar FE-SEM images of the HER catalyst (i.e., electroplated Ni) before and after the HER. In this case, we did not observe any notable change in the surface morphology of HER catalyst.

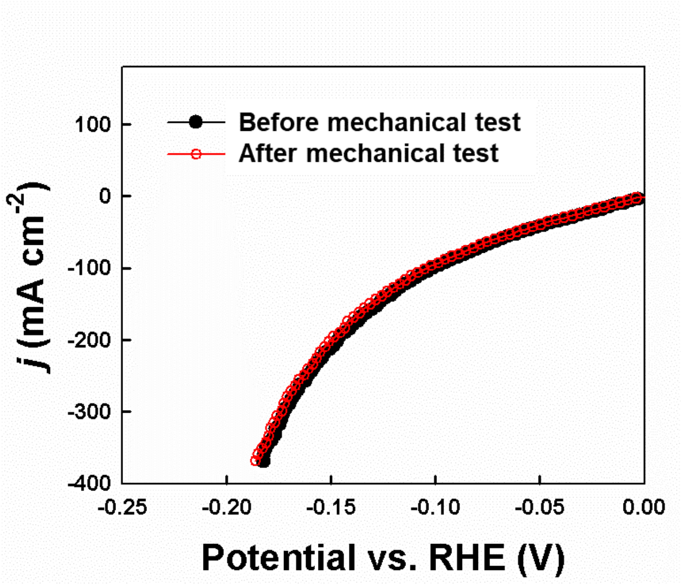

**Figure S20.** Linear sweep voltammograms (LSVs) of the EP NiFe LDH/Ni–cotton electrode before and after mechanical stability tests. In this case, the mechanical tests were repeatedly conducted by 5,000 bending cycles at a radius of ~0.3 cm).

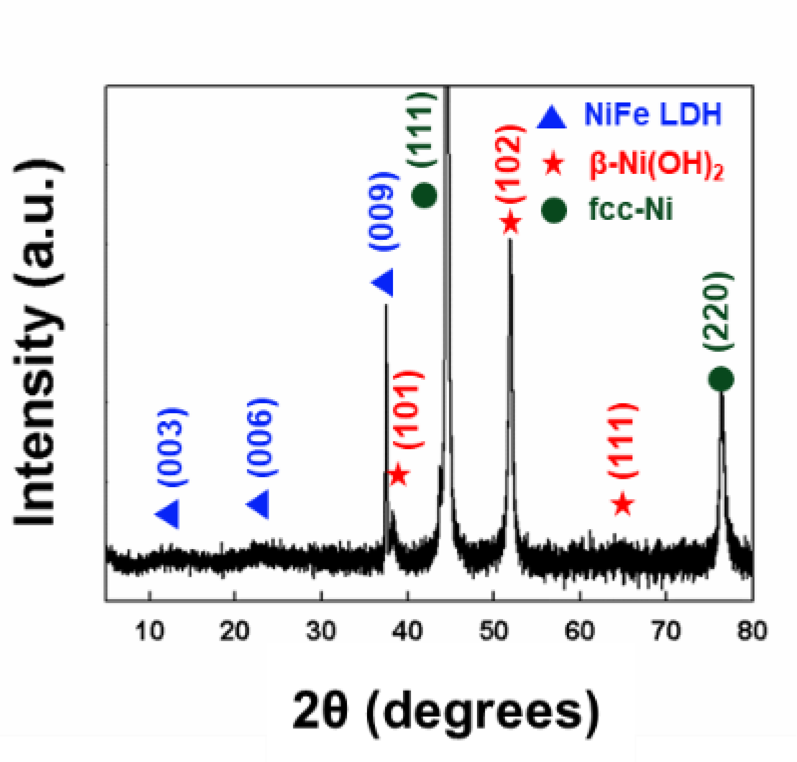

**Figure S21.** The XRD pattern of the NiFe exhibited (003), (006), and (009) peaks that were readily assigned to NiFe LDH. By contrast, the (101), (102), (111), and (220) peaks originated from the buried EP Ni sublayer (i.e., the (101), (102), and (111) peaks of β-$Ni(OH)_2$ and the (220) peak of fcc-Ni).[S2]

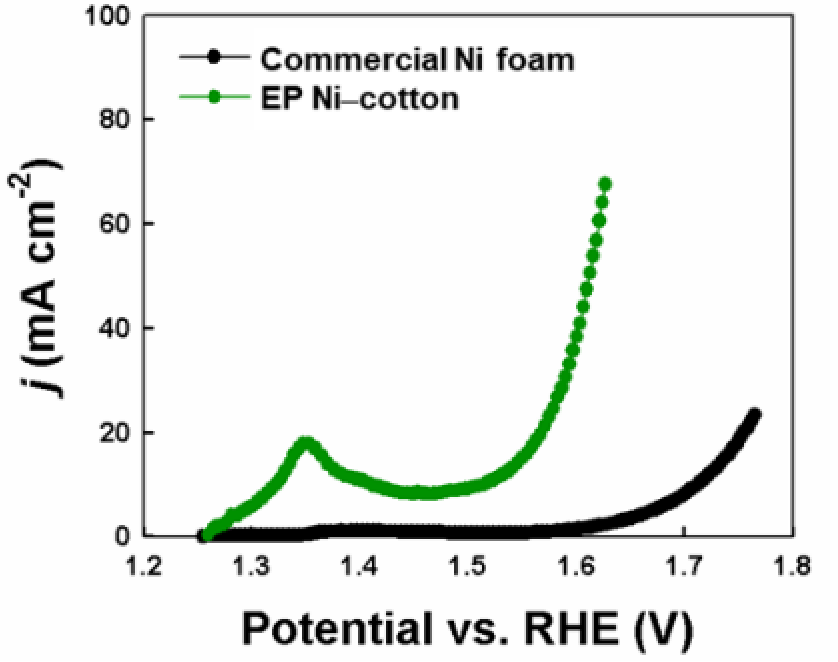

**Figure S22.** OER polarization curve of the electrodes. The anodic current density of the EP Ni–cotton showed an anodic shoulder in the low potential range of 1.3–1.4 V, arising from the conversion of Ni(II) to Ni(III).

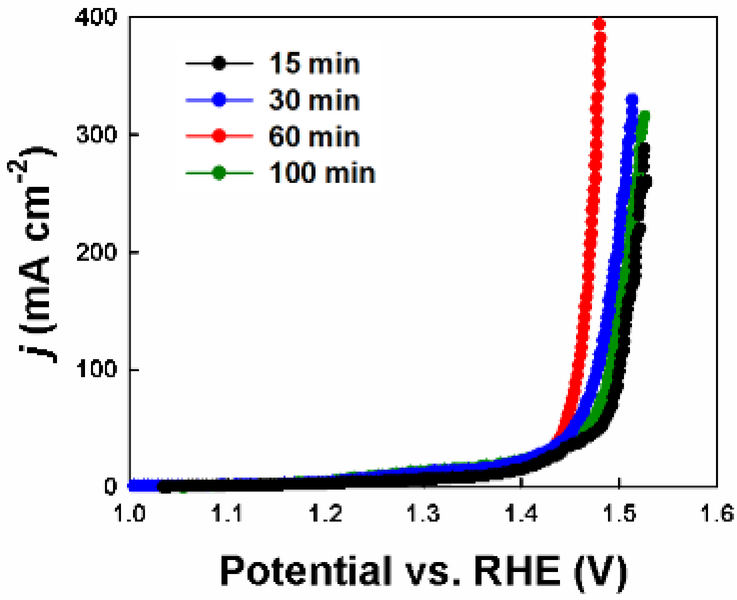

**Figure S23.** Comparison of OER polarization curves according to NiFe electroplating times.

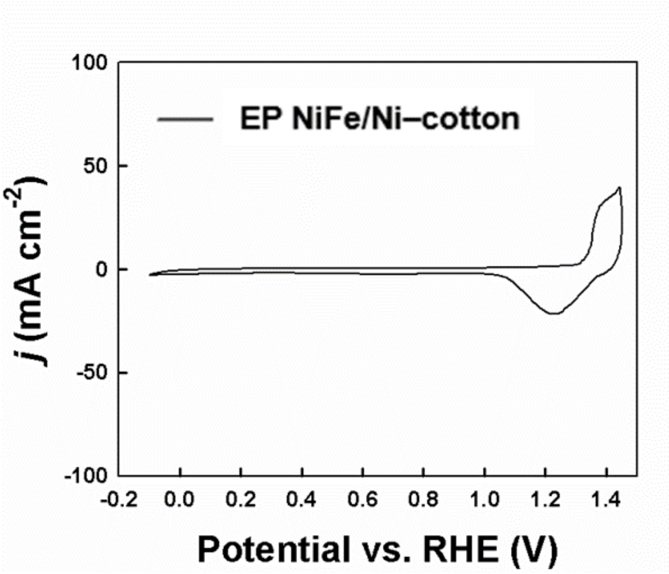

**Figure S24.** CV scan of the EP NiFe–cotton electrode in the full range of potential.

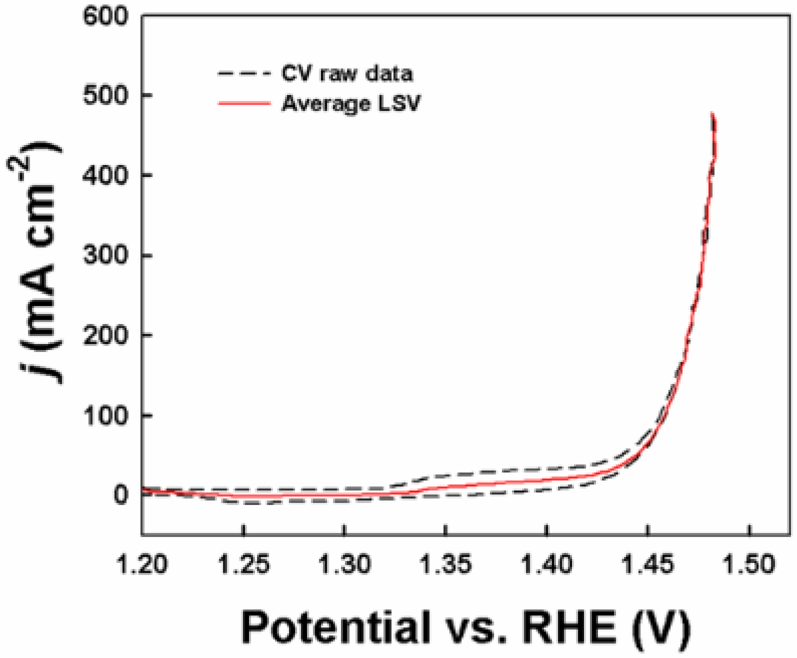

**Figure S25.** CV curves of the electrodes. OER polarization curve (red) of the EP NiFe–cotton electrode obtained from averaging the current densities of the forward and backward sweeps (black) at a scan rate of 1 mV s$^{-1}$. The anodic current density of the EP Ni–cotton showed an anodic shoulder in the low potential range of 1.3–1.4 V, arising from the conversion of Ni(II) to Ni(III) (i.e., conversion from $Ni(OH)_2$ to NiOOH).

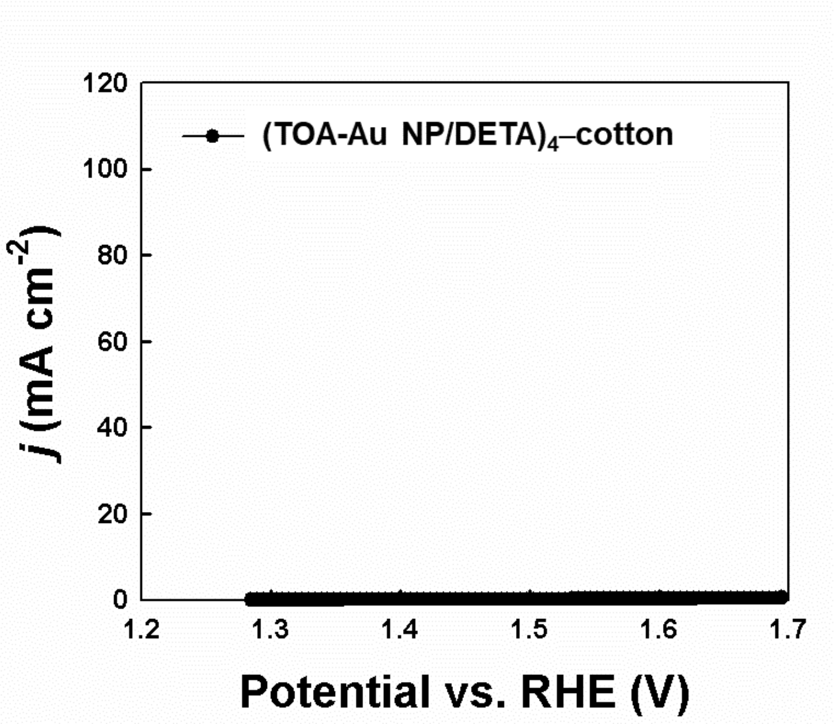

**Figure S26.** OER polarization curve of the (TOA-Au NP/DETA)$_4$-coated cotton electrode obtained in Ar-saturated 1 M KOH.

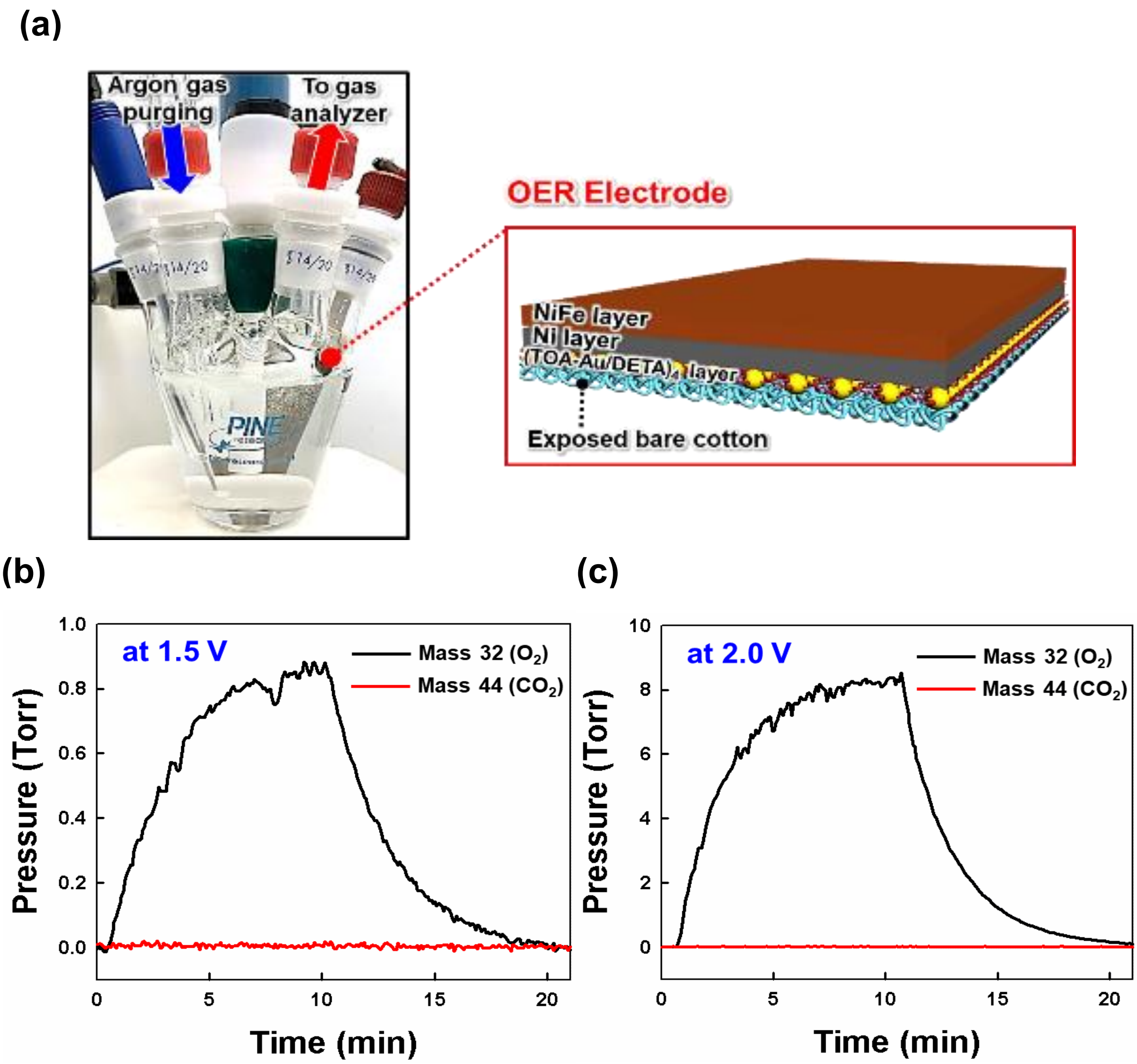

**Figure S27.** a) The photograph of carbon corrosion test cell and schematic of the OER electrode. Mass spectra of $CO_2$ and $O_2$ of OER electrode for carbon corrosion analysis at b) 1.5 V and c) 2.0 V vs. RHE. Corrosion test was conducted by applying constant potential of 1.5 V and 2.0 V (vs. RHE) to the OER electrode for 10 min. $CO_2$ emission during the corrosion test, which is direct evidence of carbon corrosion, was quantified as a function of time using mass spectrometry. Despite the presence of exposed cotton layer after cutting, $CO_2$ or CO gas was not detected in the corrosion test, indicating that carbon corrosion did not occur in the OER electrode.

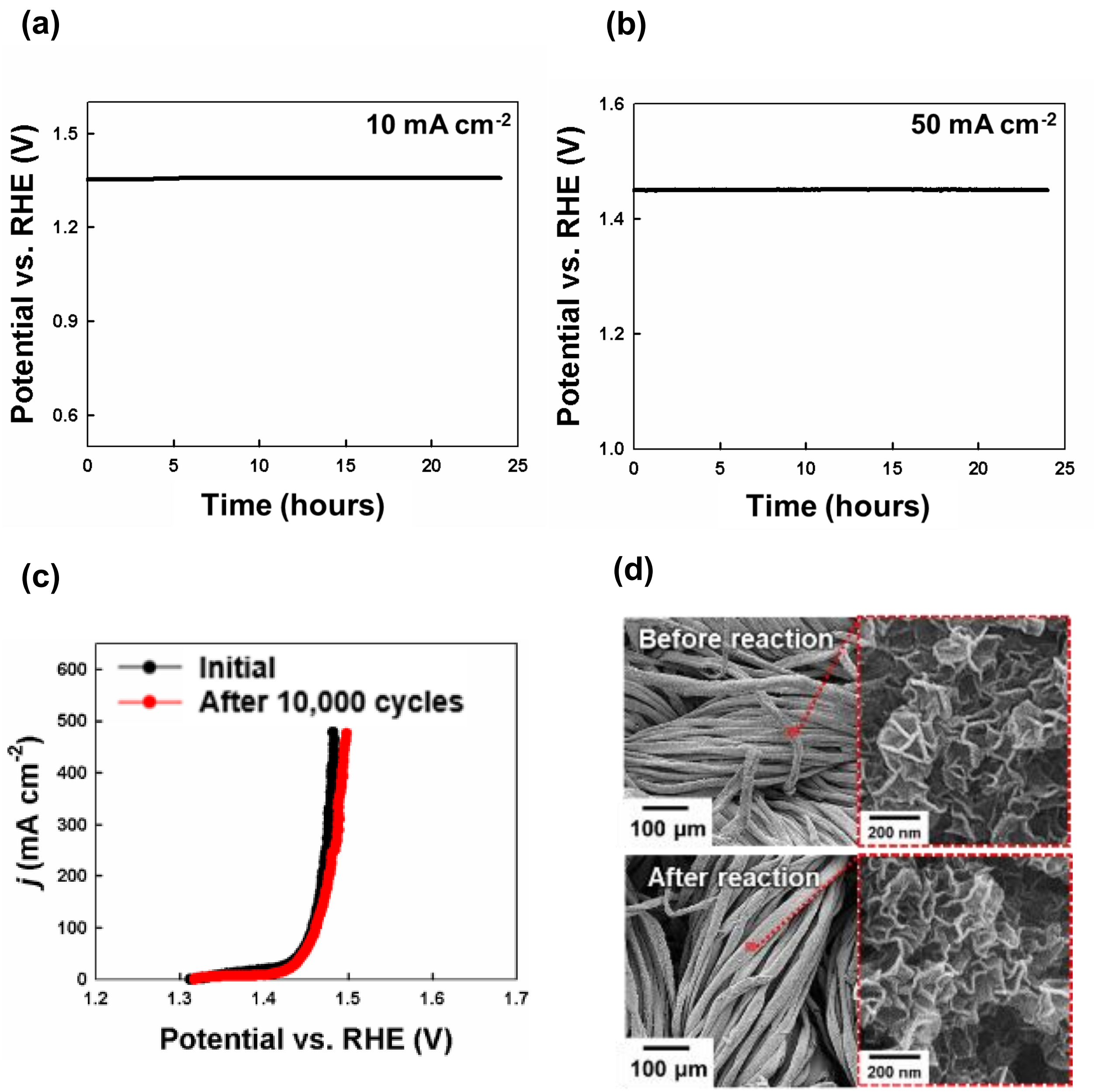

**Figure S28.** Stability test of the electrode. Chronopotentiometry curve for the EP NiFe–cotton electrode (i.e., the OER electrode) obtained at a current density of a) 10 mA cm$^{-2}$ and b) 50 mA cm$^{-2}$, and c) their polarization curves measured before and after 10,000 cycles of potential sweeping. d) FE-SEM images of the EP NiFe LDH/Ni–cotton catalyst before and after the chronopotentiometry stability test (at 10 mA cm$^{-2}$).

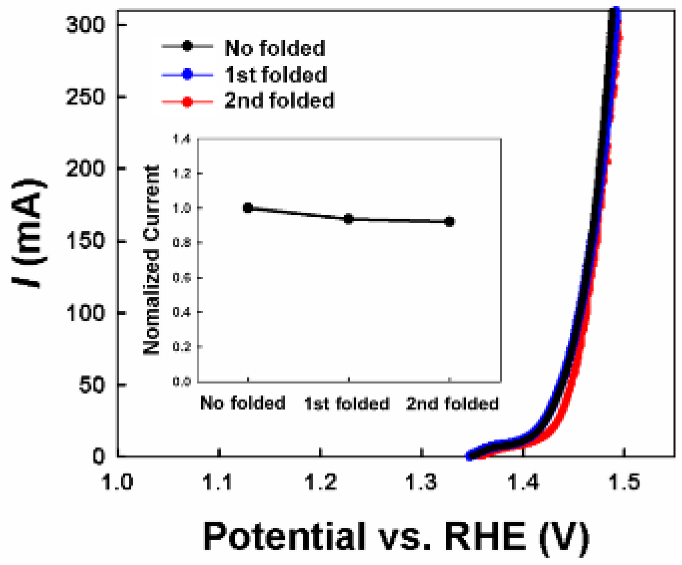

**Figure S29.** Linear sweep voltammograms (LSVs) currents of the EP NiFe LDH/Ni–cotton electrode according to the folded states. The inset shows the variation of OER at 1.49 V. In this case, the current of the unfolded electrode is normalized to 1.

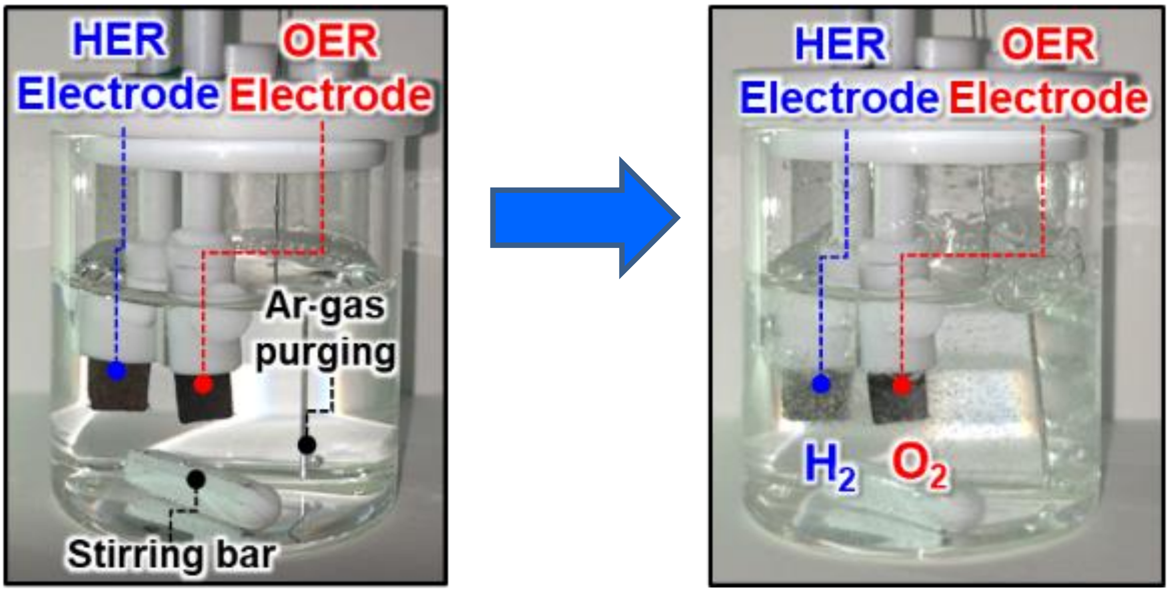

**Figure S30.** Photograph of two-electrode water electrolysis test cell composed of the EP Ni‖EP NiFe LDH/Ni–cotton textile. Hydrogen and oxygen gases are generated during the reaction.

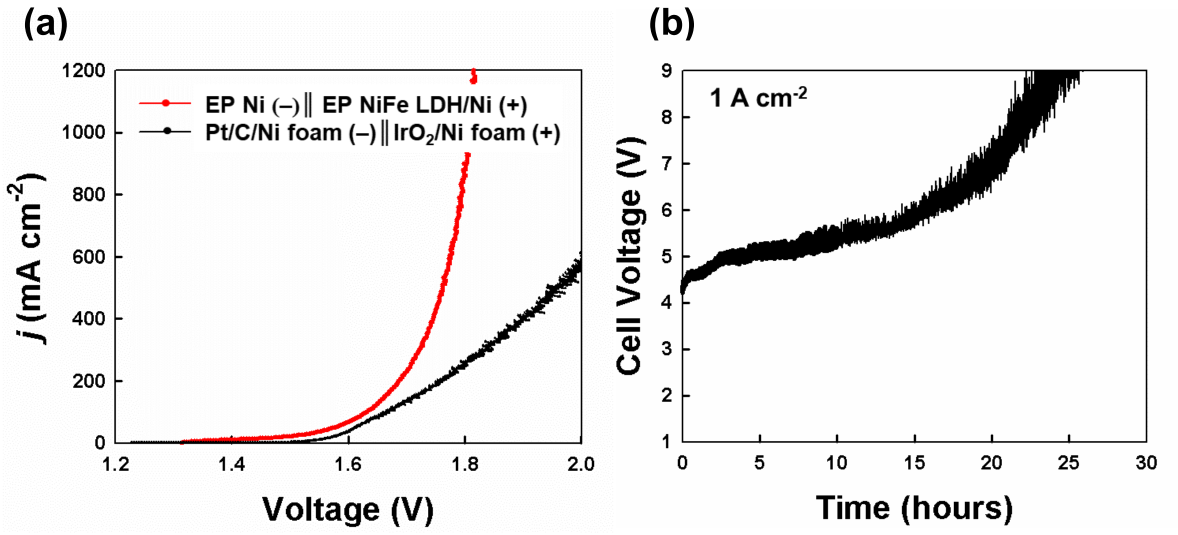

**Figure S31.** Water splitting performance of commercial Pt/C/Ni foam (-)‖IrO$_2$/Ni foam (+). a) Polarization curve of the EP Ni–cotton‖EP NiFe LDH/Ni–cotton, and Pt/C/Ni foam (-)‖IrO$_2$/Ni foam (+) electrodes. b) Chronopotentiometry curve of the Pt/C/Ni foam (-)‖IrO$_2$/Ni foam (+) electrode recorded at 1 A cm$^{-2}$. In this case, the commercial Pt/C/Ni foam (-)‖IrO$_2$/Ni foam (+) electrode exhibited considerably low operation stability compared to our cotton-based electrodes.

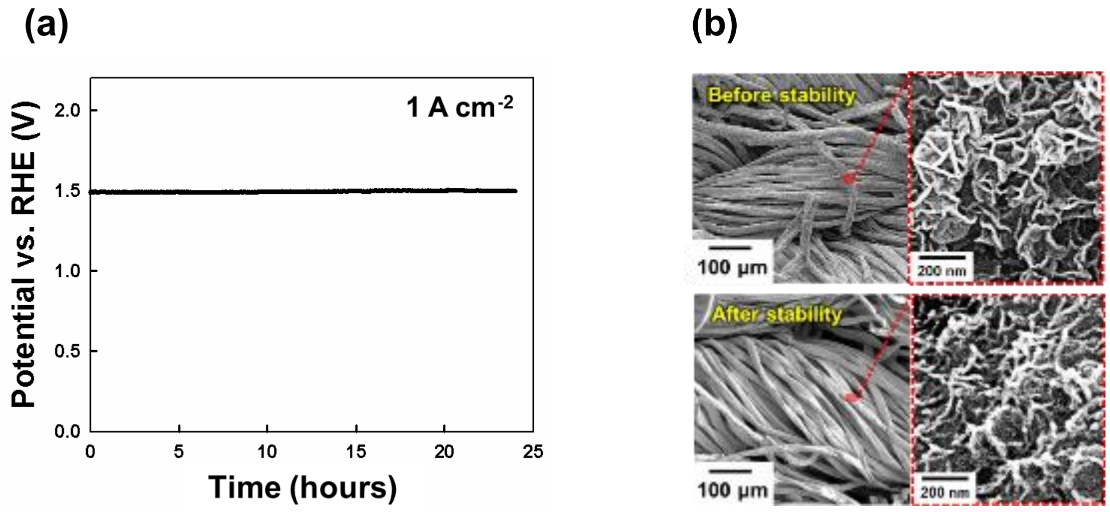

(c)

| Elements | Ni | Fe |
|---|---|---|
| | Not detected | Not detected |

**Figure S32.** Stability test of the OER electrode. a) Chronopotentiometry curve for EP NiFe/Ni–cotton electrode (i.e., the OER electrode) obtained at the current density of 1 A cm$^{-2}$ for 24 h in 1 M KOH. b) Planar FE-SEM images of the OER catalyst before and after stability test, and c) inductively coupled plasma optical emission spectrometry (ICP-OES) data of electrolyte after stability test.

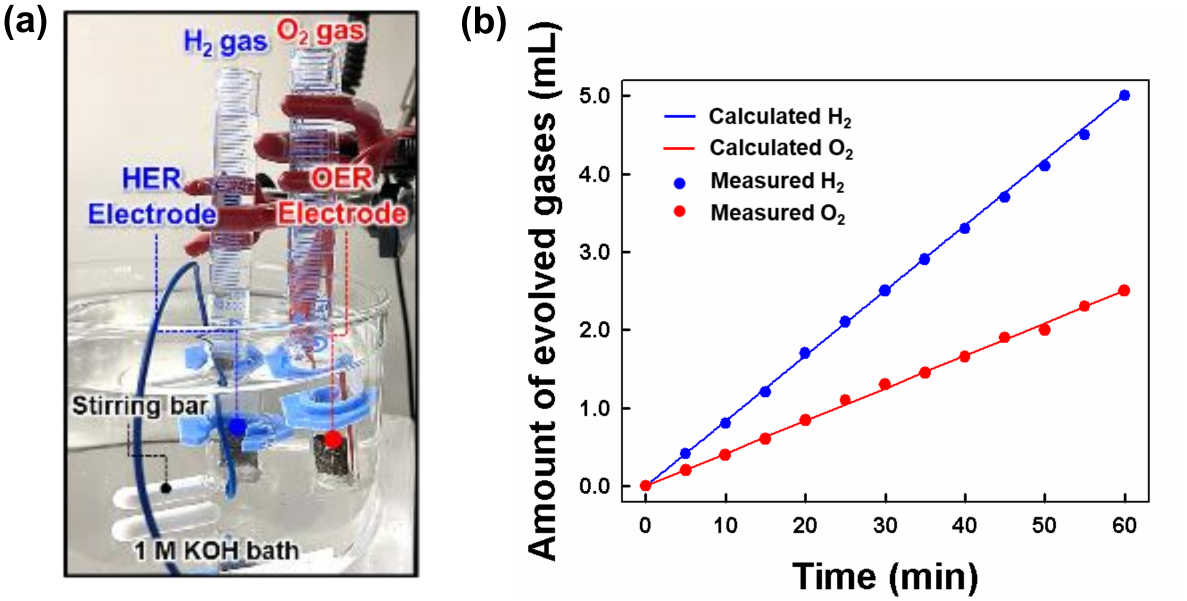

**Figure S33.** Faradaic efficiency for the overall water splitting. a) The photograph image of experimental set-ups of water displacement for collection of the evolved gas. b) The amount of theoretically calculated and experimentally measured $H_2$ and $O_2$ gases of EP Ni‖EP NiFe LDH/Ni–cotton textile as a function of interval time. In this case, faradaic efficiency for the overall water splitting at a constant current density of 10 mA cm$^{-2}$ was estimated to be approximately 99.7 %.

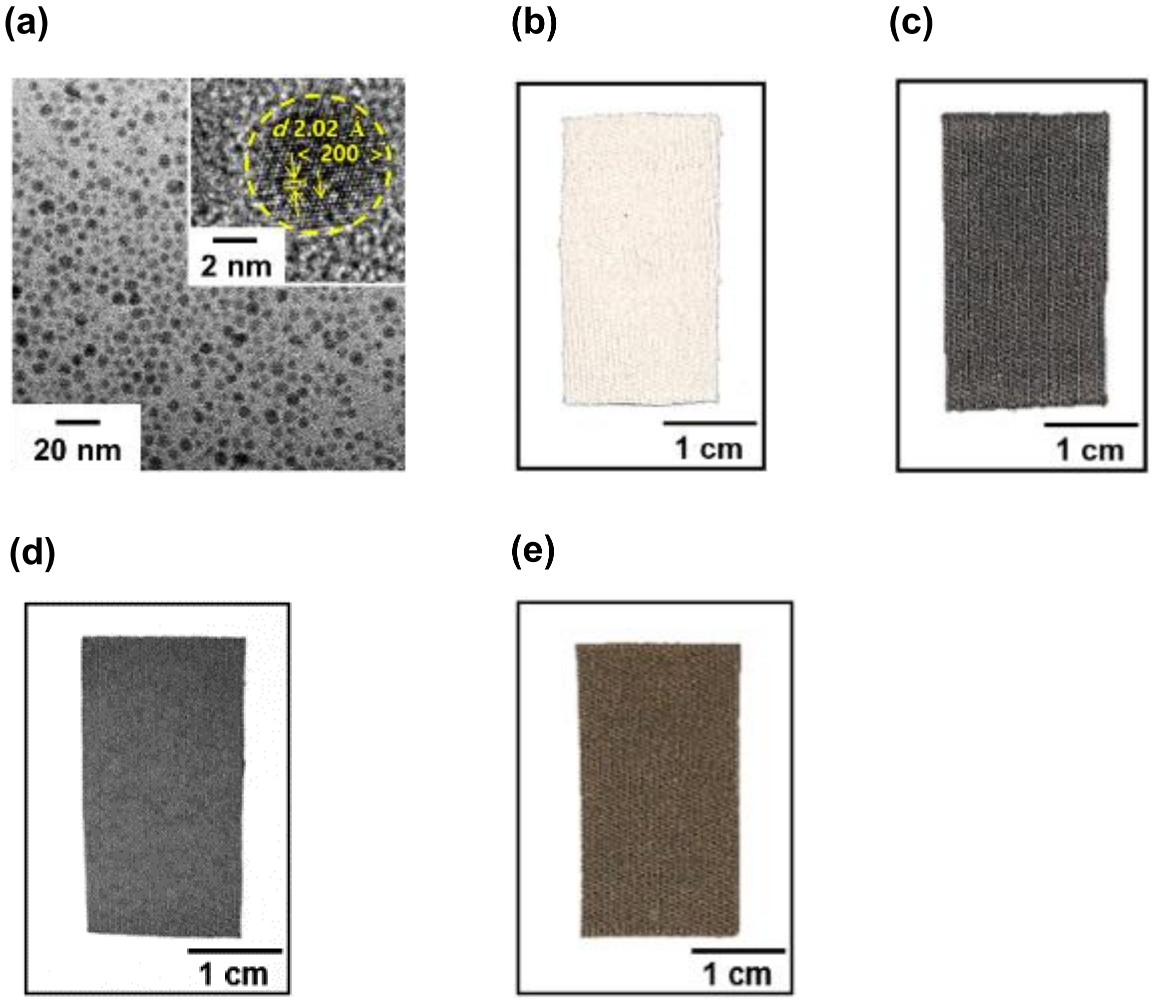

**Figure S34.** a) High-resolution transmission electron microscopy (HR-TEM) image of TOA-Ag NPs dispersed in toluene (the inset shows the lattice spacing of TOA-Ag NP). Photograph of b) bare cotton, c) conductive cotton textile prepared by ligand-exchange reaction-induced LbL-assembly between TOA-Ag NPs and DETA. d) Ni electroplated-cotton electrode, and e) NiFe LDH/Ni electroplated cotton electrode.

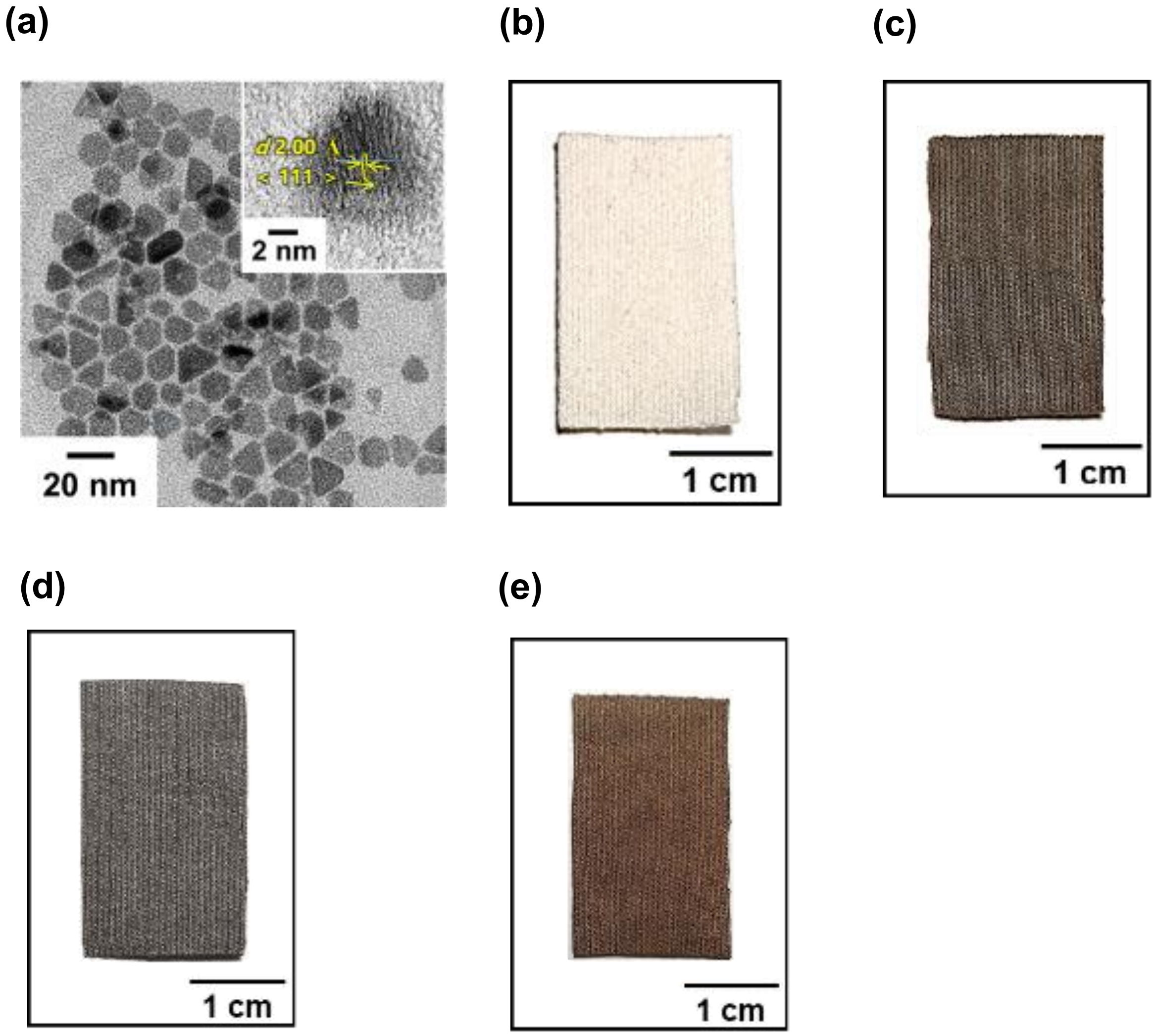

**Figure S35.** a) HR-TEM image of TOA-Cu NPs dispersed in toluene (the inset shows the lattice spacing of TOA-Cu NP). Photograph of b) bare cotton, c) conductive cotton textile prepared by ligand-exchange reaction-induced LbL-assembly between TOA-Cu NPs and amine functionalized linkers (herein, cysteamine was used as a linker instead of DETA). d) Ni electroplated-cotton electrode, and e) NiFe LDH/Ni electroplated cotton electrode.

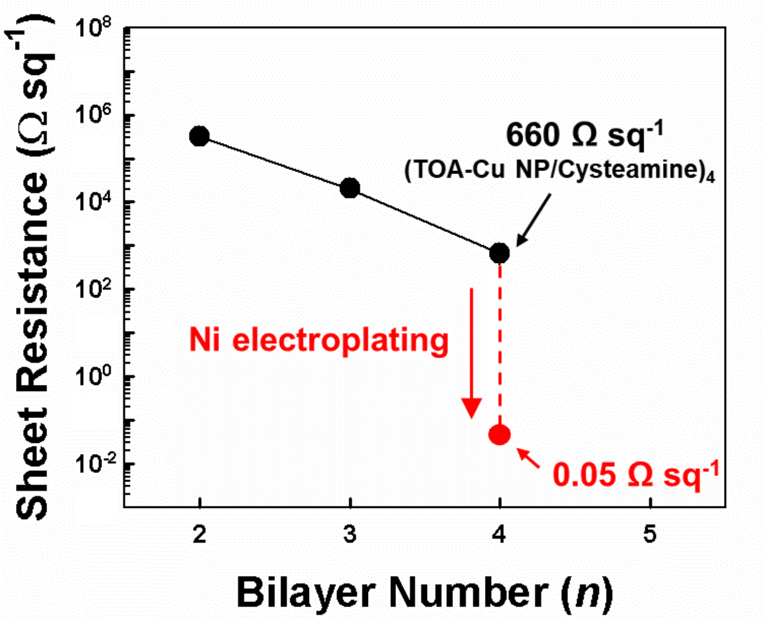

**Figure S36.** Electrical properties of electroplated Ni-coated cotton. Conductive cotton textile was first prepared by ligand-exchange reaction-induced LbL-assembly of TOA-Cu NPs and amine functionalized cysteamine.

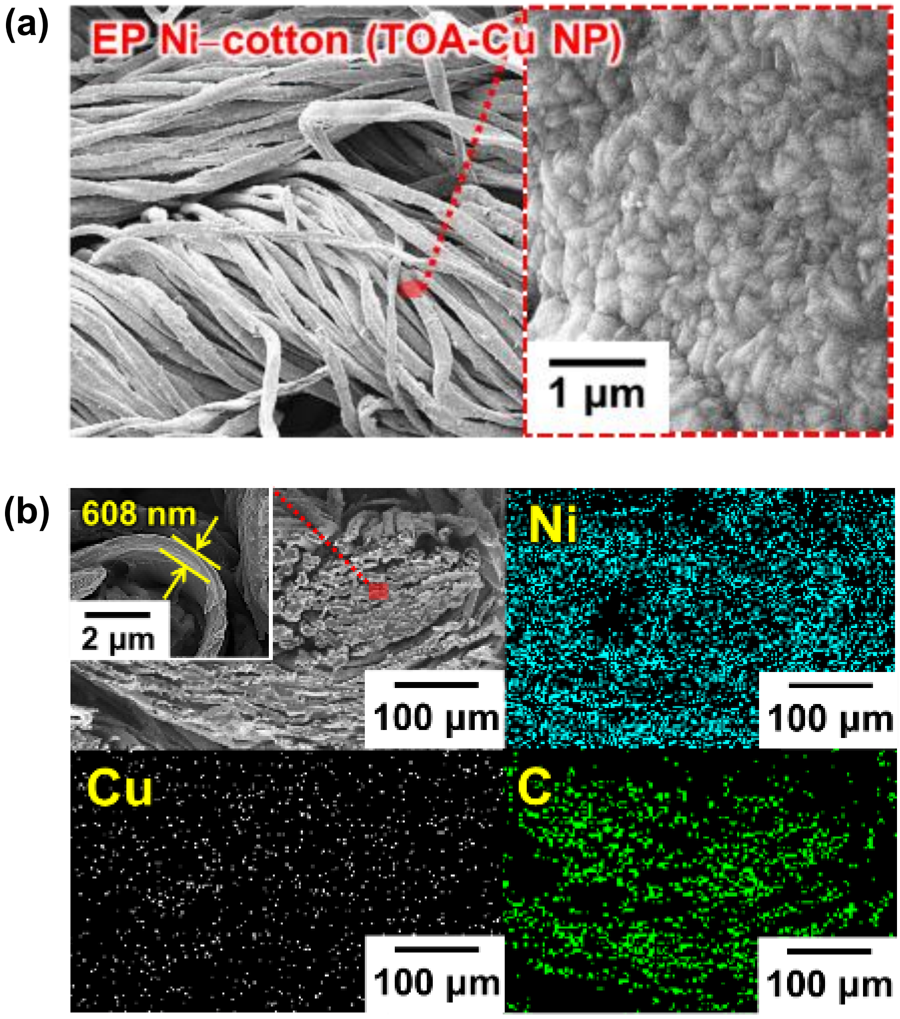

**Figure S37.** a) Planar FE-SEM images and b) cross-sectional FE-SEM image and energy-dispersive X-ray spectroscopy (EDX) mapping image of the EP Ni–cotton electrode using TOA-Cu NPs instead of TOA-Au NPs (the inset of the top-left panel shows the thickness of the EP Ni layer).

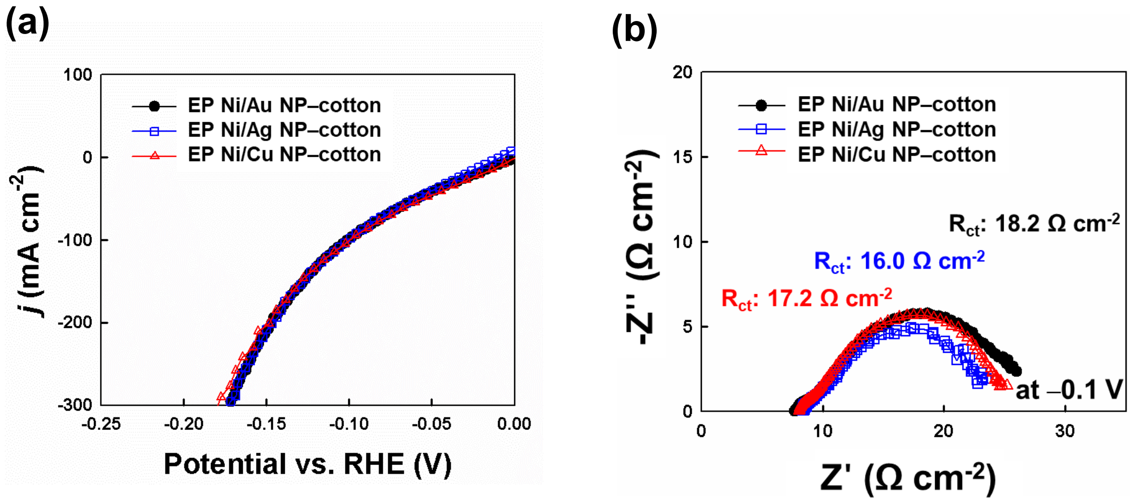

**Figure S38.** a) HER polarization curves of the EP Ni–Au NP–cotton (i.e., EP Ni–(TOA-Au NP/DETA)$_4$-coated cotton), EP Ni–Ag NP–cotton (i.e., EP Ni–(TOA-Ag NP/DETA)$_{10}$-coated cotton), and EP Ni–Cu NP–cotton (i.e., EP Ni–(TOA-Cu NP/cysteamine)$_4$-coated cotton) electrodes. b), EIS plots for the EP Ni–Au NP–cotton, EP Ni–Ag NP–cotton and EP Ni–Cu NP–cotton electrodes at an applied potential of −0.1 V (vs. RHE). The resulting HER performance of the EP Ni–cotton electrode based on TOA-Ag NP and TOA-Cu NP were almost identical to that of the EP Ni–cotton based on TOA-Au NP. In the case of TOA-Cu NPs, a cysteamine linker ($M_w \sim 77.15$ g mol$^{-1}$) was used as a molecular linker instead of DETA because Cu NPs were dissolved in DETA solution.

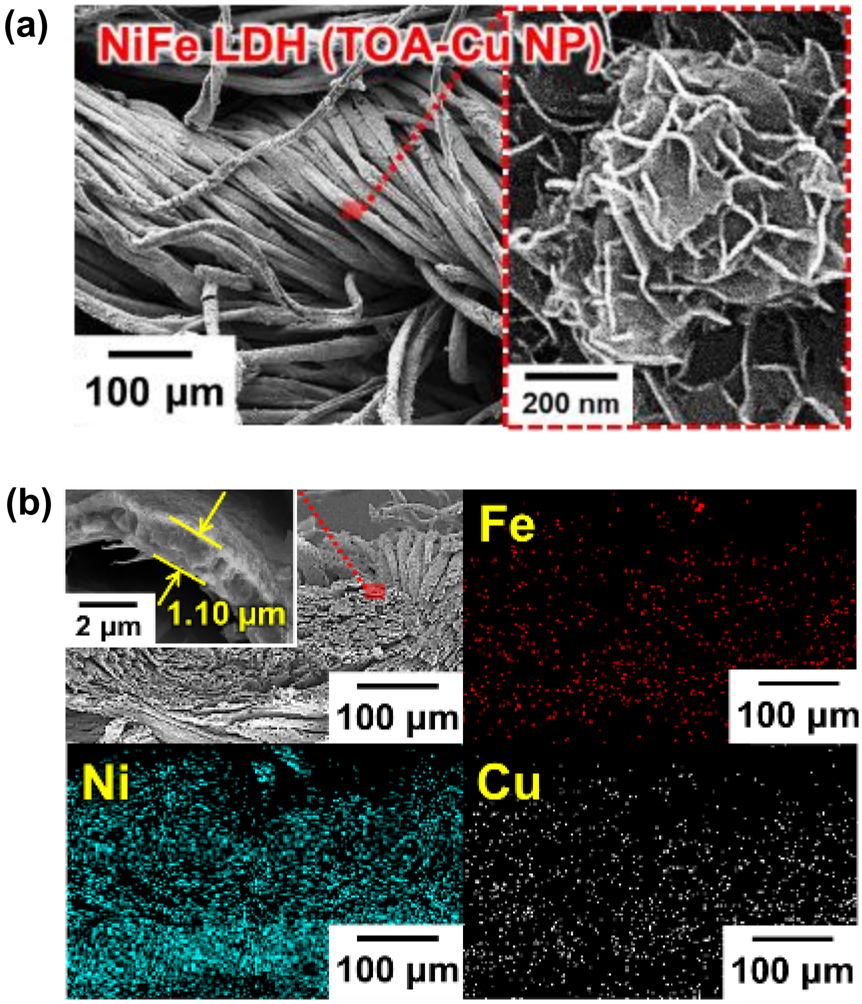

**Figure S39.** FE-SEM images of the EP NiFe/Ni–Cu NP–cotton. a) Planar FE-SEM images and b) cross-sectional FE-SEM image and energy-dispersive X-ray spectroscopy (EDX) mapping image of the EP NiFe/Ni–cotton electrode using TOA-Cu NPs instead of TOA-Au NPs (the inset of the top-left panel shows the thickness of the EP NiFe/Ni layer).

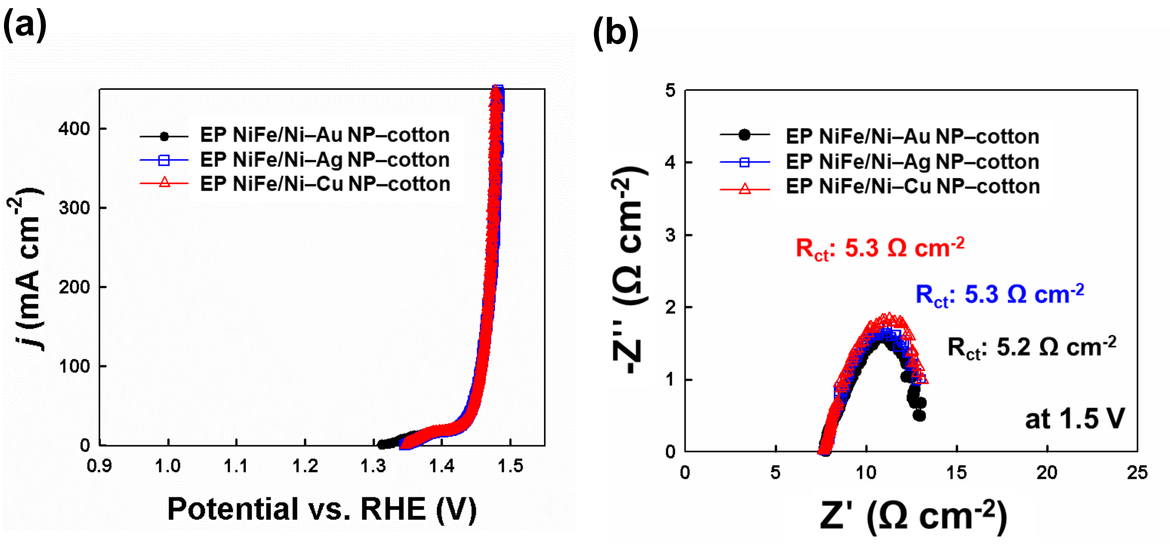

**Figure S40.** a) OER polarization curves of the EP NiFe/Ni–Au NP–cotton (i.e., EP NiFe/Ni–(TOA-Au NP/DETA)$_4$-coated cotton), EP NiFe/Ni–Ag NP–cotton (i.e., EP NiFe/Ni–(TOA-Ag NP/DETA)$_{10}$-coated cotton), and EP NiFe/Ni–Cu NP–cotton (i.e., EP NiFe/Ni–(TOA-Cu NP/cysteamine)$_4$-coated cotton) electrodes. b) EIS plots for the EP NiFe/Ni–Au NP–cotton, EP NiFe/Ni–Ag NP–cotton and EP NiFe/Ni–Cu NP–cotton electrodes at an applied potential of +1.5 V (vs. RHE). The resulting OER performances of the EP NiFe/Ni–cotton electrodes based on TOA-Ag NP and TOA-Cu NP multilayers were almost identical to that of the EP NiFe/Ni–cotton based on TOA-Au NP multilayers. In the case of TOA-Cu NP multilayers, a cysteamine linker ($M_w$ ~ 77.15 g mol$^{-1}$) was used as a molecular linker instead of DETA because Cu NPs were dissolved in DETA solution.

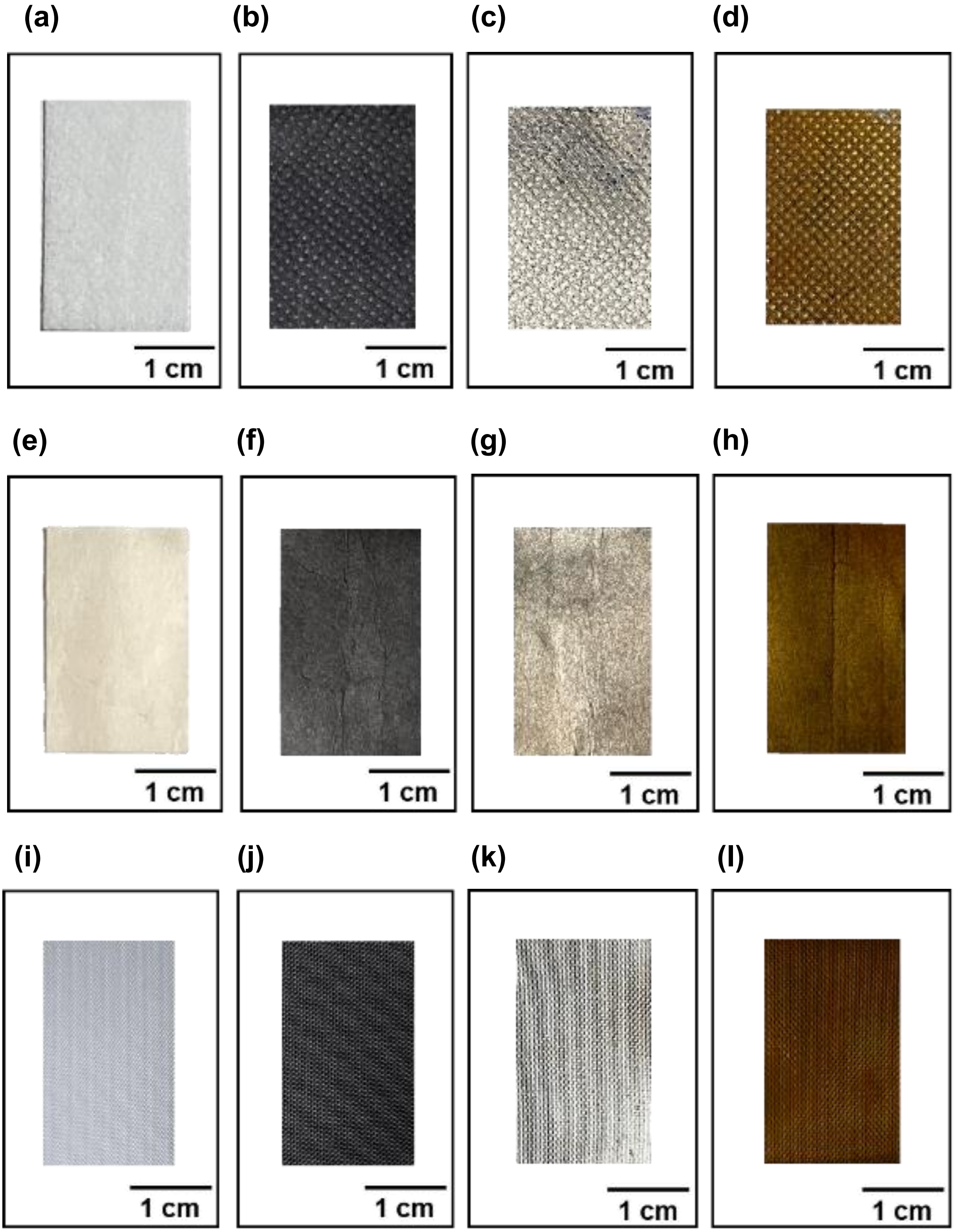

**Figure S41.** The photographic images of a) bare polyester, b) conductive polyester textile prepared from the (TOA-Cu NP/cysteamine)$_4$ multilayers, c) Ni electroplated-polyester electrode prepared from b) and d) NiFe electroplated-polyester electrode prepared from c).

The photographic images of e) bare paper, f) conductive paper textile prepared from the (TOA-Cu NP/cysteamine)$_4$ multilayers, and g) Ni electroplated-paper electrode prepared from f) and h) NiFe electroplated-paper electrode prepared from g). The photographic images of i) bare nylon, j) conductive nylon textile prepared from the (TOA-Cu NP/cysteamine)$_4$ multilayers, and k) Ni electroplated-paper electrode prepared from i) and l) NiFe electroplated-paper electrode prepared from k).

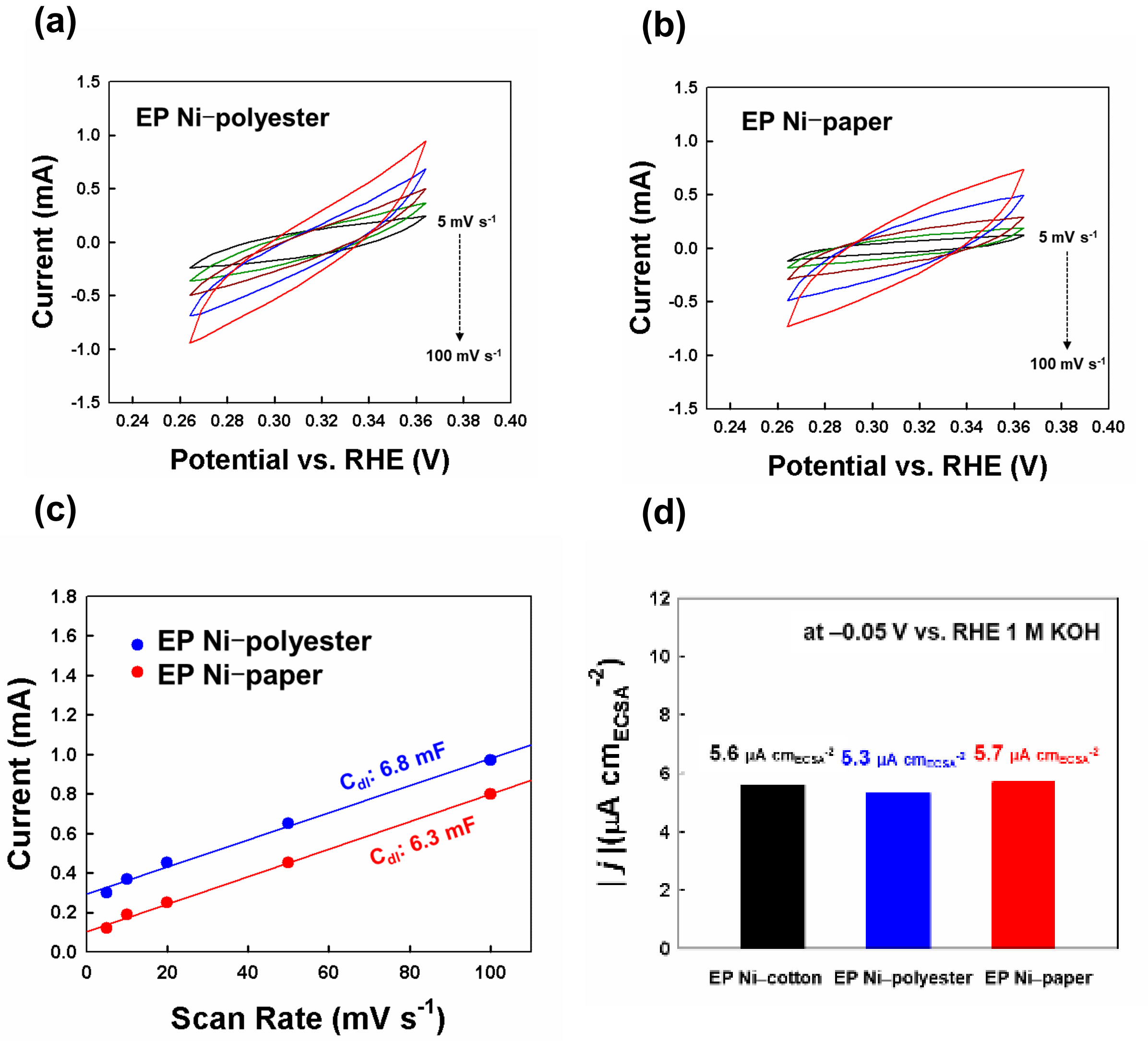

**Figure S42.** CV curves recorded in the non-faradaic region (0.26–0.36 V) at different scan rates (5, 10, 20, 50 and 100 mV $s^{-1}$) for a) EP Ni–polyester and b) EP Ni–paper. c) Double-layer capacitance ($C_{dl}$) for the electrodes measured at different scan rates. d) Intrinsic HER activity (μA $cm^{-2}_{ECSA}$) of EP Ni-coated polyester and paper electrodes normalized with respect to the ECSAs of the electrocatalysts. In this case, |*j*| is defined as the absolute value of the current density normalized with respect to the ECSAs. In this case, it should be noted that the ECSA value depends on the thickness of the substrate. Therefore, only if the Ni catalyst layer is introduced in the same method (i.e., LbL assembly-induced electroplating approach), the catalyst performance per ECSA is almost similar irrespective of substrate thickness and type.

**Table S1.** Performance comparison of Ni-based HER electrodes.

| **Catalyst** | **Overpotential (mV)** | **Tafel plot (mV dec$^{-1}$)** | **Reference** |
|---|---|---|---|
| **EP Ni–cotton textile** | **12 @10 mA cm$^{-2}$** | **32.7** | **Our work** |
| NiFe(oxo) hydroxide/ Ni-P/octet-truss polymer | 243 @10 mA cm$^{-2}$ | 141 | [S3] |
| FeNi-MOF/ commercial Ni foam | 79 @10 mA cm$^{-2}$ | 30.1 | [S4] |
| FeP/$Ni_2P$/ commercial Ni foam | 14 @10 mA cm$^{-2}$ | 24.2 | [S5] |
| $Ni_{11}(HPO_3)_8(OH)_6$/ commercial Ni foam | 121 @10 mA cm$^{-2}$ | 102 | [S6] |
| $Ni_3N$-NiMoN/ carbon cloth | 31 @10 mA cm$^{-2}$ | 64 | [S7] |
| N-$Ni_3S_2$/ commercial Ni foam | 110 @10 mA cm$^{-2}$ | - | [S8] |
| NiFe LDH/Cu NW[a]/ commercial Cu foam | 116 @10 mA cm$^{-2}$ | 58.9 | [S2] |
| NiS/Ni/ commercial Ni foam | 130 @10 mA cm$^{-2}$ | 58.5 | [S9] |
| $NiCo_2S_4$ NF[b]/ commercial Ni foam | 140 @10 mA cm$^{-2}$ | 84.5 | [S10] |
| $NiCo_2S_4$ NWs[a]/ commercial Ni foam | 210 @10 mA cm$^{-2}$ | 58.9 | [S11] |

[a] NW: nanowire; [b] NF: nanoflake.

**Table S2.** Performance comparison of Ni-based OER electrodes.

| **Catalyst** | **Overpotential (mV)** | **Tafel plot (mV dec$^{-1}$)** | **Reference** |
|---|---|---|---|
| **EP NiFe LDH/ Ni–cotton textile** | **214 @50 mA cm$^{-2}$**<br>**228 @100 mA cm$^{-2}$** | **27** | **Our work** |
| FeNi-MOF/ commercial Ni foam | 235 @50 mA cm$^{-2}$ | 55.4 | [S4] |
| $Ni_{11}(HPO_3)_8(OH)_6$/ commercial Ni foam | 364 @100 mA cm$^{-2}$ | 91 | [S6] |
| N-$Ni_3S_2$/ commercial Ni foam | 330 @100 mA cm$^{-2}$ | 70 | [S8] |
| NiFe LDH/Cu NW[a)]/ commercial Cu foam | 281 @100 mA cm$^{-2}$ | 27.8 | [S2] |

[a)] NW: nanowire.

**Table S3.** Performance comparison of Ni-based overall water splitting electrodes.

| HER catalyst (Cathode) | OER catalyst (Anode) | Voltage (V) | Reference |
|---|---|---|---|
| **EP Ni–cotton textile** | **EP NiFe LDH/<br>Ni–cotton textile** | **1.39 @10 mA cm$^{-2}$** | **Our work** |
| FeNi-MOF/<br>commercial Ni foam | FeNi-MOF/<br>commercial Ni foam | 1.50 @10 mA cm$^{-2}$ | [S4] |
| FeP/$Ni_2P$/<br>commercial Ni foam | FeP/$Ni_2P$/<br>commercial Ni foam | 1.42 @10 mA cm$^{-2}$ | [S5] |
| $Ni_{11}(HPO_3)_8(OH)_6$/<br>commercial Ni foam | $Ni_{11}(HPO_3)_8(OH)_6$/<br>commercial Ni foam | 1.6 @10 mA cm$^{-2}$ | [S6] |
| $Ni_3N$-NiMoN/<br>carbon cloth | $Ni_3N$-NiMoN/<br>carbon cloth | 1.54 @10 mA cm$^{-2}$ | [S7] |
| N-$Ni_3S_2$/ commercial<br>Ni foam | N-$Ni_3S_2$/commercial<br>Ni foam | 1.48 @10 mA cm$^{-2}$ | [S8] |
| NiFe LDH/<br>Cu NW[a)]/<br>commercial Cu foam | NiFe LDH/<br>Cu NW[a)]/<br>commercial Cu foam | 1.54 @10 mA cm$^{-2}$ | [S2] |
| $NiCo_2S_4$ NWs[a)]/<br>commercial Ni foam[a)] | $NiCo_2S_4$ NWs[a)]/<br>commercial Ni foam | 1.63 @10 mA cm$^{-2}$ | [S11] |

[a)] NW: nanowire.

## References

[S1] X. Yu, J. Zhao, L.-R. Zheng, Y. Tong, M. Zhang, G. Xu, C. Li, J. Ma, G. Shi, *ACS Energy Lett.* **2018**, *3*, 237.

[S2] L. Yu, H. Zhou, J. Sun, F. Qin, F. Yu, J. Bao, Y. Yu, S. Chen, Z. Ren, *Energy Environ. Sci.* **2017**, *10*, 1820.

[S3] X. Su, X. Li, C. Y. A. Ong, T. S. Herng, Y. Wang, E. Peng, J. Ding, *Adv. Sci.* **2019**, *6*, 1801670.

[S4] D. Senthil Raja, H.-W. Lin, S.-Y. Lu, *Nano Energy* **2019**, *57*, 1.

[S5] F. Yu, H. Zhou, Y. Huang, J. Sun, F. Qin, J. Bao, W. A. Goddard, S. Chen, Z. Ren, *Nat. Commun.* **2018**, *9*, 2551.

[S6] P. W. Menezes, C. Panda, S. Loos, F. Bunschei-Bruns, C. Walter, M. Schwarze, X. Deng, H. Dau, M. Driess, *Energy Environ. Sci.* **2018**, *11*, 1287.

[S7] A. Wu, Y. Xie, H. Ma, C. Tian, Y. Gu, H. Yan, X. Zhang, G. Yang, H. Fu, *Nano Energy* **2018**, *44*, 353.

[S8] P. Chen, T. Zhou, M. Zhang, Y. Tong, C. Zhong, N. Zhang, L. Zhang, C. Wu, Y. Xie, *Adv. Mater.* **2017**, *29*, 1701584.

[S9] G.-F. Chen, T. Y. Ma, Z.-Q. Liu, N. Li, Y.-Z. Su, K. Davey, S.-Z. Qiao, *Adv. Funct. Mater.* **2016**, *26*, 3314.

[S10] L. Ma, Y. Hu, R. Chen, G. Zhu, T. Chen, H. Lv, Y. Wang, J. Liang, H. Liu, C. Yan, H. Zhu, Z. Tie, Z. Jin, J. Liu, *Nano Energy* **2016**, *24*, 139.

[S11] A. Sivanantham, P. Ganesan, S. Shanmugam, *Adv. Funct. Mater.* **2016**, *26*, 4660.